SANDIA REPORT

SAND2001-3645
Unlimited Release
Printed December 2001

High Al-Content AlInGaN Devices for Next Generation Electronic and Optoelectronic Application

Albert G. Baca, Ronald D. Briggs, Andrew A. Allerman, Christine C. Mitchell, Carol I. Ashby, Alan F. Wright, Randy J. Shul

Prepared by
Sandia National Laboratories
Albuquerque, New Mexico 87185 and Livermore, California 94550

Sandia is a multiprogram laboratory operated by Sandia Corporation, a Lockheed Martin Company, for the United States Department of Energy under Contract DE-AC04-94AL85000.

Approved for public release; further dissemination unlimited.

Sandia National Laboratories

Issued by Sandia National Laboratories, operated for the United States Department of Energy by Sandia Corporation.

NOTICE: This report was prepared as an account of work sponsored by an agency of the United States Government. Neither the United States Government, nor any agency thereof, nor any of their employees, nor any of their contractors, subcontractors, or their employees, make any warranty, express or implied, or assume any legal liability or responsibility for the accuracy, completeness, or usefulness of any information, apparatus, product, or process disclosed, or represent that its use would not infringe privately owned rights. Reference herein to any specific commercial product, process, or service by trade name, trademark, manufacturer, or otherwise, does not necessarily constitute or imply its endorsement, recommendation, or favoring by the United States Government, any agency thereof, or any of their contractors or subcontractors. The views and opinions expressed herein do not necessarily state or reflect those of the United States Government, any agency thereof, or any of their contractors.

Printed in the United States of America. This report has been reproduced directly from the best available copy.

Available to DOE and DOE contractors from
U.S. Department of Energy
Office of Scientific and Technical Information
P.O. Box 62
Oak Ridge, TN 37831

Telephone: (865)576-8401
Facsimile: (865)576-5728
E-Mail: reports@adonis.osti.gov
Online ordering: http://www.doe.gov/bridge

Available to the public from
U.S. Department of Commerce
National Technical Information Service
5285 Port Royal Rd
Springfield, VA 22161

Telephone: (800)553-6847
Facsimile: (703)605-6900
E-Mail: orders@ntis.fedworld.gov
Online order: http://www.ntis.gov/ordering.htm

SAND2001-3645
Unlimited Release
Printed November 2001

High Al-Content AlInGaN Devices for Next Generation Electronic and Optoelectronic Applications

Albert G. Baca and Ronald D. Briggs
RF Microsystems Technology Department

Andrew A. Allerman and Christine C. Mitchell
Chemical Processing Science Department

Arthur J. Fischer
Semiconductor Materials and Device Sciences Department

Carol I. H. Ashby
Sensor Technologies Department

Alan F. Wright
Nanostructure and Chemical Physics Department

Randy J. Shul
Microdevice Technologies Department

Sandia National Laboratories
P. O. Box 5800
Albuquerque, NM 87185-0603
Contact: Albert Baca, 505-844-7127, agbaca@sandia.gov

Abstract

Great strides have been made in the development of ultraviolet LED materials and devices. Power levels in the near UV (below 390 nm) have been improved from the 10 μW to the 1 mW level through improvements in the growth and design of AlInGaN alloys. High frequency AlGaN/GaN HEMTs have been developed with f_t *of 65 GHz and* f_{max} *of 85 GHz, all while attaining breakdown voltage greater than 100 V. A new breakthrough in the lateral overgrowth of GaN materials promises to further improve these devices.*

Acknowledgments

The authors acknowledge several key contributors to this project who have since left Sandia. Jung Han did the initial development of AlInGaN alloy material and Mary Crawford did much of the early work in UV LEDs. We would also like to acknowledge, Dave Follstaedt, Joel Wendt, Cedric Monier, Marcelino Armendariz, Steve Lee, Sean Hearne, Weng Chow, Sam Myers, Jeff Fiegel, Paula Provencio, Nancy Missert, Karen Waldrip, Lei Zhang, Mike Banas, Melissa Cavaliere, Gerry Lopez, and Leo Griego for their technical contributions.

Contents

I. **Introduction ………………………………………………………** **7**

II. **Cantilever Epitaxy: A Method for Low-Dislocation- ………. Density GaN from a Single Growth on a Textured Substrate** **9**

III. **Mechanisms of Cracking in AlGaN Materials Grown ……… on GaN** **13**

IV. **The Effects of Biaxial Strain and Chemical Ordering ……… on the Band Bap of InGaN** **21**

V. **MOCVD Growth of Quaternary (Al,Ga,In)N for UV ……… Optoelectronics** **27**

VI. **Study of In-Containing UV LED Alloy Material ……………** **37**

VII. **Design and Performance of Nitride-based UV LEDs ……….** **43**

A. Internal Absorption Effects for Shorter Wavelength (λ < 370 nm) UV LEDs
B. AlGaN Cladding Designs: Critical thickness Limitations and Carrier Leakage
C. Performance of GaN/AlGaN MQW LEDs for λ < 360 nm

VIII. **AlGaN/GaN HEMTs …………………………………………….** **51**

IX. **References ……………………………………………………..** **57**

Figures

1. Cross-section SEM micrograph of cantilever epitaxy…………………….... 9
2. 10 kV CL image of CE showing partial absence of TDs (dark regions) ….. along coalescence fronts (arrows). 10
3. Cross-section TEM image of cantilever epitaxy obtained using weak beam **g**=$[11\bar{2}0]$ conditions. 10
4. AFMs comparing effect of support:trench ratio. Dark spots indicate …….. presence of mixed vertical threading dislocations. 11
5. SEM image of a 0.5μm $Al_{0.37}Ga_{0.63}N$ on 0.7μm of GaN heterostructure on Sapphire. Overgrowth of cracks was common in the films we examined (circled region). (inset) Dark field optical plan view image of the crack network in an $Al_{0.17}Ga_{0.83}N$ film. 14
6. Stress-thickness plot of a 0.5μm $Al_{0.17}Ga_{0.83}N$ on 0.7μm of GaN film (not shown). The dot indicates the critical thickness. 15
7. Bright-field XTEM image of dislocations in $Al_{0.37}Ga_{0.63}N$/GaN, using two-beam diffraction conditions with **g** = (11-20); [1-100] specimen tilted 30° about [11-20] axis to broaden the projected image of the interface. 17
8. Plot of critical thickness versus $1/\sigma^2$ for six samples (squares). The line is the fracture critical thickness (eq. 3) using the Northup surface-energy values. 18
9. Measured gap deviations for strained wurtzite and unstrained zinc-blende InGaN. The gap deviations are computed using measured band gaps for unstrained wurtzite and zinc-blende GaN from the corresponding references, and assuming band gaps of 1.89 eV for wurtzite InN and 1.80 eV for zinc-blende InN. 22
10. Calculated gap deviations for random unstrained wurtzite InGaN, ……… estimated gap deviations for zinc-blende InGaN, and corresponding experimental results for zinc-blende InGaN. The symbols for the wurtzite results show the average of the gaps from the five configurations and the vertical lines give the standard deviations. 23
11. Calculated and experimental gap deviations for wurtzite. The symbols for the wurtzite results show the average of the gaps from the five configurations and the vertical lines give the standard deviations. Note that we have offset the compositions for the random results by ± 0.003 to make them easier to distinguish. 24
12. An RBS spectrum from an AlGaInN sample. The solid line is a simulated fit. 28
13. PL of GaInN epilayers with various amount of Indium. The integrated …. intensity increases by more than 10 times from GaN to 4% GaInN. 29
14. the GaN lattice parameter. The (0002) GaN diffraction peaks move ……. progressively toward higher-angle side as the lattice parameters of the upper alloy layers reduce. 30

15. Room-temperature photoluminescence from a GaN (solid line) epilayer … and two AlGaInN epilayers (samples d and f). 31
16. Contour plot of constant (in-plane) lattice parameter and emission energy versus Al and In compositions for AlGaInN epilayers. 32
17. (0002) 2θ-ω x-ray diffraction of an AlGaInN (100Å)/GaInN (45Å) ……… multiple (10) quantum wells. 33
18. Cross-sectional TEM image of an AlGaInN (100Å)/GaInN (45Å) multiple (10) quantum wells. 34
19. In-situ stress measurement of during growth of an MQW LED…………… 34
20. Temperature-dependent PL (at 10, 75, 150, and 295 K with decreasing ….. intensity) suggesting an internal quantum efficiency of around 20% from the AlGaInN/GaInN MQWs. 35
21. Schematic of UV LED MQW heterostructures……………………………. 38
22. (a) Room temperature PL spectra of InGaN bulk epilayers and (b) ………. Temperature dependent integrated PL intensity of InGaN bulk epilayers with In composition x. The Ea values are derived from fitting the data to equation 1. 39
23. (a) T=10K PL of InGaN, GaN and AlGaN MQWs and (b) Temperature … dependence of peak PL intensity for InGaN, GaN and AlGaN MQWs. 40
24. EL spectra for AlGaN MQW LED at various injection currents………… 44
25. (a) Top view photograph of a GaN /AlGaN MQW barrier and (b) I-V …. characteristics for several cracked GaN LED with > 0.2 μm total thickness of $Al_{0.2}Ga_{0.8}N$/AlGaN MQW LEDs. 45
26. Schematic of the GaN SQW heterostructure and states involved in the ….. carrier leakage model. 46
27. Electron (solid curve) and hole (dashed curve) densities in unconfined …. states versus total (confined and unconfined) carrier population at T=300K for (a) 2 nm GaN QW/$Al_{0.1}Ga_{0.9}N$ barrier structure and (b) 4 nm GaN QW/$Al_{0.1}Ga_{0.9}N$ barrier structure. 47
28. Electron (solid curve) and hole (dashed curve) densities in unconfined ….. states versus total (confined and unconfined) carrier population as a function of temperature for (a) 2 nm GaN QW/$Al_{0.1}Ga_{0.9}N$ barrier structure and (b) 2 nm GaN QW/$Al_{0.2}Ga_{0.8}N$ barrier structure. A total carrier concentration of $1x10^{11}$ cm^{-2} was assumed. 48
29. (a) Electroluminescence spectrum of 30 Å GaN/AlGaN MQW LED at 5 ... mA. (b) Light output-current-voltage characteristic for this 120 μm diameter mesa-etched device. 49
30. (a) Electroluminescence spectrum of a GaN/AlGaN MQW LED at 20 ….. mA. (b) Light output-current-voltage data for this device. 50
31. (a) Electroluminescence spectrum of InGaN/AlInGaN MQW LED at 20 .. mA. (b) Light output-current-voltage data for this device. 51
32. Drain I-V characteristics for a 0.25x150 $μm^2$ GaN HEMT……………………… 52
33. Drain I-V and g_m for a 0.25x150 $μm^2$ GaN HEMT……………………………… 52
34. Transconductance plots for 0.1, 0.25, and 0.5 μm gate length GaN ……… 53

HEMTs.
35. Measured cutoff frequency and maximum frequency of oscillation for 0.1x100 μm^2 GaN HEMTs. 53
36. Gate length-ft product for various GaN HEMTs………………………….... 54
37. Microwave power performance of a 0.25x150 μm^2 GaN HEMT at 3 GHz……… 54

Introduction

Tremendous recent breakthroughs in the technology of GaN and related AlGaInN materials synthesis and device demonstrations have sparked worldwide interest in these materials for lighting and electronic applications. High brightness LEDs are now commercially available in red, green, and blue colors. The latter color utilizes (Ga,In)N alloys. These LEDs are enabling new types of multi-color displays, among other applications. "White" LEDs are also commercially available, by means of using a blue LED whose light output impinges on a phosphor. The resulting light lacks proper color balance in part due to the lack of emission at shorter wavelengths than that of the blue LED (420 nm) and in part due to the fact that commercial phosphors have been optimized for the UV emission lines of atomic mercury.

The potential of LEDs exists to provide more fuel efficient light sources than the ubiquitous incandescent and fluorescent bulbs. Because lighting consumes 7% of the world's energy, energy savings alone can be huge. In order for LEDs to be considered for lighting applications, improvements are needed in the efficiency and cost. The efficiency of the initial "white" LED was only 5 lumens/watt. In order to improve the efficency and versatility of solid-state light sources, migration to shorter wavelengths is needed. By adding Al and In to GaN the energy bandgap can be tuned from the visible (2.0 eV) to the ultraviolet (UV, 6.1 eV). Prior to the start of this project, the shortest wavelength UV LED had just been demonstrated by Sandia National Laboratories. This In-free LED emitted at a wavelength of 355 nm but had a low power level 2-3 orders of magnitude less that blue LEDs. These results suggest that In plays a key role in the brightness of nitride-based LEDs, which needs to be better understood. Further improvements in high-Al content AlGaInN materials and devices were needed in order to realize efficient solid-state white light illumination.

Portable communications systems for the military or satellites have much higher power transmission requirements than commercial wireless systems, resulting in heavy and buldy systems. Likewise, higher power output levels are critical to increase range and discrimination in military radars, particularly phased array and synthetic aperture radars. For many systems such high power levels will come with unacceptable size, weight, and cost if the vacuum tube power sources cannot be replaced by solid-state sources. GaN with its large bandgap (3.4 eV), high breakdown field (> 3x106 V/cm) and saturation drift velocity (2.5 x 107 cm/s), and chemical inertness will enable a new generation of high power electronics critical for many defense and commercial applications.

Conventional solid-state devices such as metal-semiconductor-metal field effect transistors (MESFETs), high electron mobility transistors (HEMTs), and heterojunction bipolar transistors (HBTs) that operate at commercial voltages of 10 V or less can be designed for higher power levels but will result in extremely low output impedance levels that result in matching networks that dominate system size. High breakdown voltage is the key to reducing the size and complexity of impedance matching networks that can reduce

the size and complexity of these systems. With high voltage operation, more reasonable impedance levels can be achieved for power levels in excess of 10 watts which result in simpler and smaller matching networks. GaN/AlGaN materials are a natural solution because their high breakdown field allows high breakdown voltage without excessively increasing the transit length and thus reducing the maximum frequency of operation. For this reason, we undertook the development of high Al content HEMTs to address these needs.

At the start of this project there had been some impressive demonstrations of GaN HEMT power transistors that were predicted to exceed power output levels of 5 W/mm. However, GaN HEMTs were plagued with problems related to traps and material quality issues. For example, there are many transient effects observed in GaN HEMT operation such as a reduction in drain current from the steady state levels after application of short duration pulses that are much more severe than conventional GaAs devices. Also, the high power levels of GaN devices presented considerable thermal and reliability issues.

Both electronic and photonic devices can benefit from the development of high Al content materials, a focus of this project. However, other materials growth issues are as significant, if not more so. GaN lacks a true substrate on which to base epitaxial growth. The commonly used substrates, sapphire and silicon carbide, have lattice constants 12% and 3% from that of GaN. Growth on such substrates will generate strain in the initial stages, which is accommodated by the formation of misfit dislocations which propagate into threading dislocations as the crystal growth proceeds. The density of vertical threading dislocations typically exceeds 10^9 cm^{-2}. Such high dislocation densities, did not affect the commercialization of visible LEDs or laboratory demonstrations of high power HEMTs, but they were an impediment to the development of visible lasers. They may also play a role in many of the poorly understood transients present in GaN HEMTs.

Methods of lateral epitaxial overgrowth have been touted as possible solutions to some of these material issues. It had been demonstrated that GaN can be made to grow over a mask such as silicon dioxide in a lateral direction with a three orders of magnitude reduction in dislocation density. This process was critical in achieving good reliability for laser diodes. Nevertheless, the LEO process was complex and did not seem to produce good results for GaN HEMTs. Clearly, better methods of lateral epitaxial overgrowth were needed.

During this LDRD, methods of growth were studied for high Al to come up with ways to deal with the stress and grow AlGaInN alloys without cracking. Also the competing growth requirements for Al containing alloys and In containing alloys were studied in order to best determine how to grow quaternary alloys for device applications. A new method of lateral overgrowth was developed in order to reduce dislocation density with a simpler and more effective process. The role of In in achieving high brightness LEDs has also been studied. Finally, improved GaN HEMTs and near UV LEDs were developed. This work is detailed in the following sections of this report.

Cantilever epitaxy: a method for low-dislocation-density GaN from a single growth on a textured substrate

The density of threading dislocations (TD) in GaN grown directly on flat sapphire substrates is typically greater than $10^9/cm^2$. Such high dislocation densities degrade both the electronic and photonic properties of the material. The density of dislocations can be decreased by orders of magnitude using cantilever epitaxy (CE) [1] , which employs prepatterned sapphire substrates to provide reduced-dimension mesa regions for nucleation and etched trenches between them for suspended lateral growth of GaN or AlGaN. The substrate is prepatterned with narrow lines and etched to a depth that permits coalescence of laterally growing III-N nucleated on the mesa surfaces before vertical growth fills the etched trench. Low dislocation densities ($<10^6/cm^2$) typical of epitaxial lateral overgrowth (ELO) are obtained in the cantilever regions and the TD density can also be reduced over the support region by forming facets to redirect vertical threading dislocations (VTDs) into horizontal dislocations.

In the CE process, one first etches a suitable pattern into a substrate to a depth that will permit lateral growth to span the distance between support features before vertical growth in the etched trench regions interferes with cantilever growth. We have employed sapphire wafers in our initial work, but the concepts are equally applicable to other common GaN substrate materials, including SiC, Si(111), and $LiGaO_2$. A typical CE structure is shown in Fig. 1.

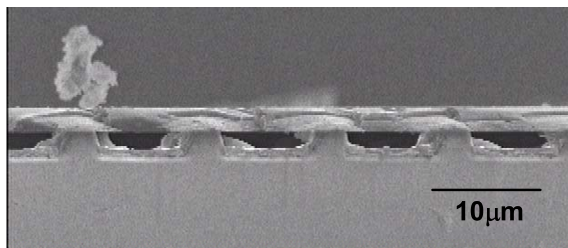

Fig. 1. Cross-section SEM micrograph of cantilever epitaxy.

A typical CE mask consists of a series of parallel lines that define mesa and trench areas. For fast cantilever growth the lines are oriented in the $<1\bar{1}00>$ direction and cantilever growth is in the $<11\bar{2}0>$ direction. Line orientation in the $<11\bar{2}0>$ direction produces slower cantilever growth in the $<1\bar{1}00>$ direction. Coalescence from CE growth in either direction can be achieved with proper selection of trench width-to-depth ratios.

Details of our metalorganic chemical vapor deposition (MOCVD) growth conditions for ELO have been previously reported [2] and were used with some modification for the CE growths. The structure in Fig. 1 was grown using a 250 Å LT-GaN nucleation layer, an intermediate later of 0.4 μm GaN grown at 1050 ºC, and cantilevers grown at 1100 ºC for enhanced lateral growth. Starting with a 2.5-μm wide support mesa,

cantilevers can be grown that are V TD-free in the cantilever, display extended VTD-free regions at the coalescence front, and display a reduced VTD density over the support on the order of 0.5 μm from the mesa edge, as shown by cathodoluminescence (Fig 2) and transmission electron microscopy (TEM) (Fig. 3).

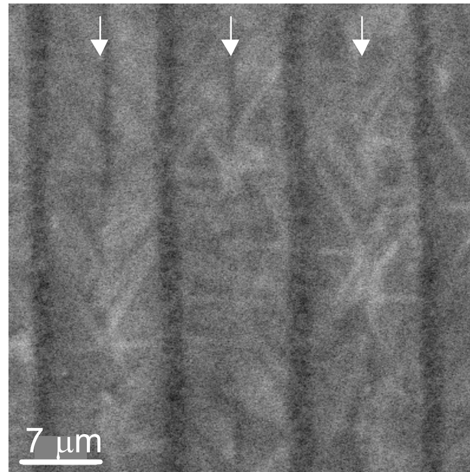

Figure 2. 10 kV CL image of CE showing partial absence of TDs (dark regions) along coalescence fronts (arrows).

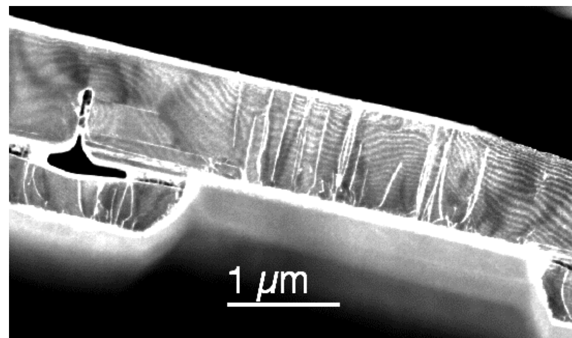

Figure 3: Cross-section TEM image of cantilever epitaxy obtained using weak beam **g**=$[11\bar{2}0]$ conditions.

Greater reduction of the total dislocation density can be achieved by using narrow supports. VTD densities in the low $10^6/cm^2$ have been obtained with a starting support/trench pattern ratio or 1:4 (Fig 4), as determined by atomic force microscopy (AFM) measurement of VTDs possessing a screw component.

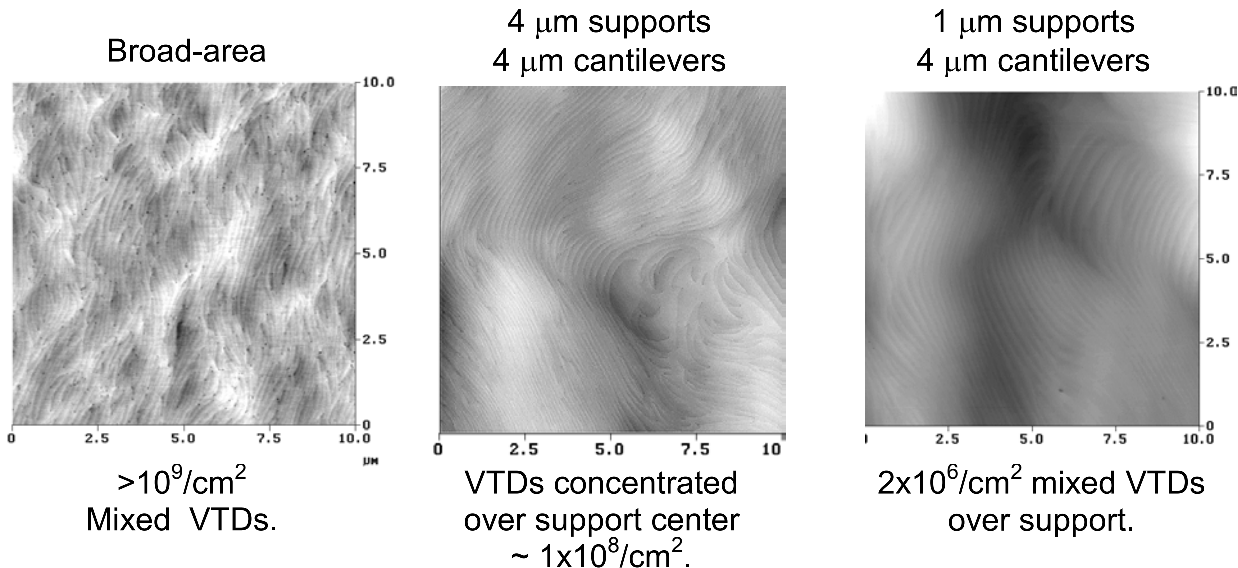

Fig. 4. AFMs comparing effect of support:trench ratio. Dark spots indicate presence of mixed vertical threading dislocations.

We have hypothesized that the redirection of VTDs into HTDs obtained near the edge of a mesa support region is due to the formation of angled wall facets near the mesa edge during growth of the intermediate layer. If the vertical growth step of the intermediate layer is performed under conditions that lead to the formation of angled facets over the entire support width, it should be possible to redirect the VTDs that normally form over the support into HTDs. Preliminary results using lower intermediate growth temperatures, which favor formation of angled facets in the $\{1\bar{1}01\}$ and $\{11\bar{2}2\}$ families of plane, have shown a reduction in VTDs over the supports, as determined by AFM.

The CE method possesses several significant advantages over conventional ELO. Most significantly, the entire structure is grown during a single growth with the different growth behavior (nucleation layer, predominantly vertical intermediate layer growth, and lateral cantilever growth) being controlled by adjustments of process variables such as temperature, pressure, and/or reactant flow rate during that single growth. ELO, in contrast, is a regrowth process with ex- situ dielectric mask deposition and patterning steps interposed between an initial GaN growth and the subsequent ELO regrowth of low dislocation density material. The reduced consumption of reactants over the dielectric mask due to selective nondeposition of GaN on the mask results in an increase reactant supply and enhanced rates in regions with large dielectric/GaN ratios. Additionally, the lateral growth rate in a given region slows with time as the overgrown GaN occupies an increasing areal fraction. In contrast, CE involves

GaN-on-GaN growth during the entire growth of the cantilever. Consequently, reactant supply should remain relatively constant and reactant-supply-derived growth-rate variations should minimized, producing negligible "fill-factor" effects for a wide range of patterns.

Perhaps the most significant advantage of CE is that is does not depend on selective nondeposition of reactants on a mask to provide a surface over which lateral overgrowth can proceed. Deposition on the dielectric mask in ELO becomes nonselective upon the addition of Al or In. Consequently, ELO can only be used for the binary GaN. In contrast, CE relies only on differences in lateral and vertical growth rates over "free space." One would expect that addition of Al-containing or In-containing reactants might alter the precise reaction conditions required to obtain enhanced lateral rates but would not preclude lateral growth and coalescence. In a preliminary growth study, AlGaN has been observed to grow in the CE mode. Consequently, CE may prove suitable for directly growing AlGaN "substrates" of a desired composition and lattice constant.

Mechanisms of Cracking in AlGaN Materials Grown on GaN

AlGaN grows in a state of tensile stress on GaN due to the difference in lattice parameters [3-7]. The high tensile coherency stress can promote catastrophic failure of the film via crack generation, which places a mechanical limitation on the device structures that can be successfully fabricated. In this work we report real-time measurements of the stress evolution during AlGaN growth on GaN using a wafer-curvature-based stress monitor incorporated onto a metal-organic chemical vapor deposition (MOCVD) reactor. In this manner we determined directly the critical thickness for cracking, and the subsequent relaxation kinetics, as a function of the growth conditions. Furthermore, we found that cracks appear to initiate the subsequent formation of misfit dislocations, which actually provides most of the observed stress relaxation.

GaN and AlGaN films were grown using an inductively heated, vertical, rotating disk reactor. Trimethylgallium, trimethylaluminum, and ammonia were the precursors, with hydrogen as the carrier gas. The films were deposited onto 2 inch diameter, 330 μm thick, (0001) basal plane sapphire wafers. All samples were grown using a standard two-step deposition process. First, a low-temperature buffer of GaN was deposited (~550°C). The wafer was then heated to 1050°C for deposition of the high-temperature (HT) films. The HT layers nominally consisted of 0.7 μm of GaN followed by the $Al_xGa_{1-x}N$ films, with thicknesses that ranged from 0.3μm to 0.7 μm and aluminum concentrations of 9% to 37% (coherency strains from 0.2 – 0.9%).

Stress evolution was measured in real-time during deposition using a multi-beam optical stress sensor (MOSS). Details of the experimental setup and analysis of the stress evolution of GaN films are provided in Ref. [8], with a general description of the MOSS technique given in Ref. [9]. MOSS measures the curvature of the film/substrate composite during deposition; the curvature is directly proportional to the product of the film stress and the film thickness (the "stress-thickness"). Following growth, the aluminum concentrations were determined by *ex-situ* x-ray diffraction (XRD), and the microstructure and morphology were characterized using secondary electron microscopy (SEM), atomic force microscopy (AFM), optical microscopy, and cross-section transmission electron microscopy (XTEM)..

Figure 5 (inset) is an optical micrograph showing the crack network in a 0.7 μm $Al_{0.17}Ga_{0.83}N$ film. This sample displays cracks nominally lying on $\{11\underline{2}0\}$ planes [10]. When the coherency stress was large (high Al content), cracks were also observed on the $\{1\underline{1}00\}$ planes (not shown). The $\{11\underline{2}0\}$ cracks typically had large (~1000Å wide) faceted openings at the surface, which is consistent with the observations of Ito *et al.* [11]. $\{1\underline{1}00\}$ cracks did not exhibit facets at the surface, but were characterized by terraced atomic steps that were closely aligned on the opposite sides of the crack, suggesting that these cracks occurred late in the film growth.

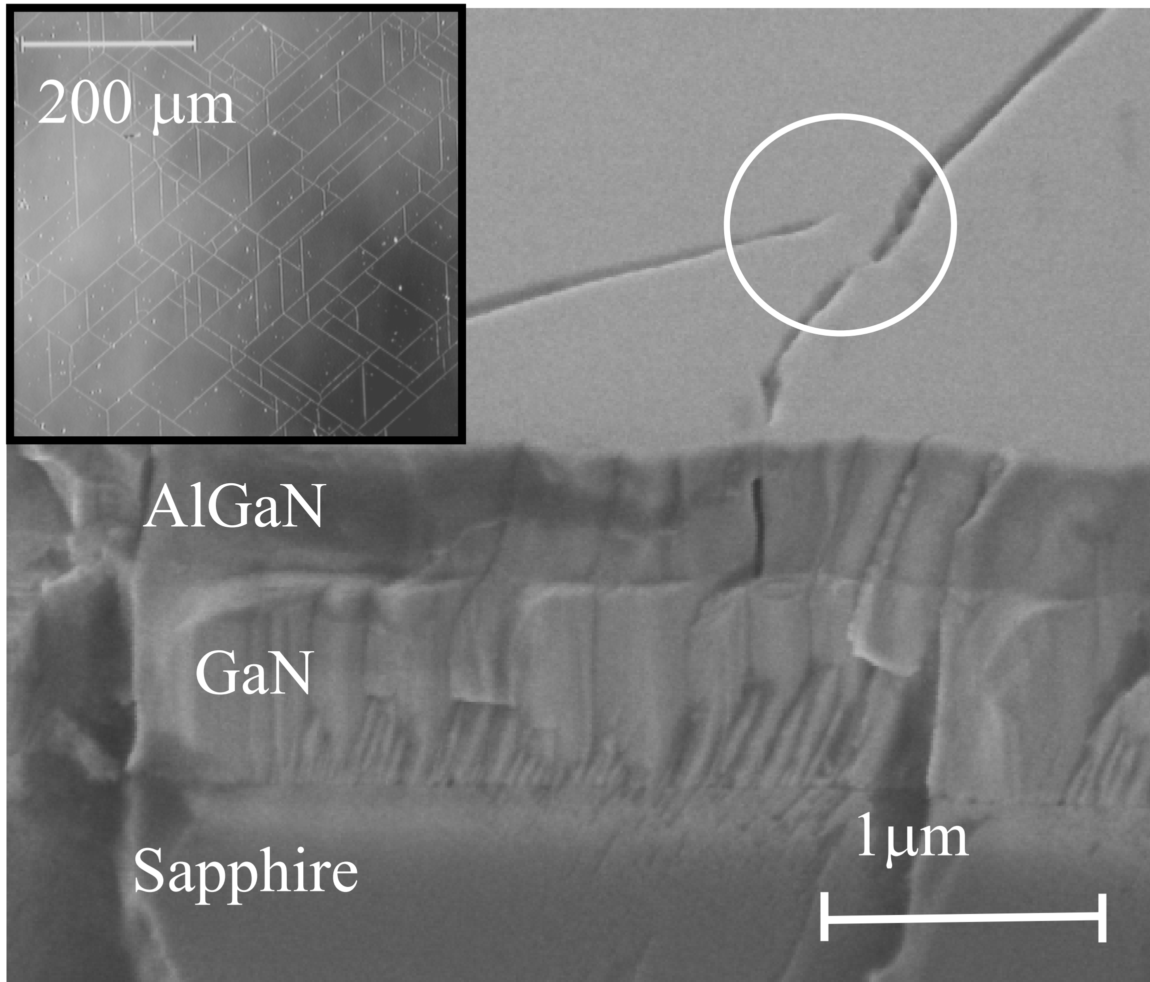

Figure 5. SEM image of a 0.5μm $Al_{0.37}Ga_{0.63}N$ on 0.7μm of GaN heterostructure on Sapphire. Overgrowth of cracks was common in the films we examined (circled region). (inset) Dark field optical plan view image of the crack network in an $Al_{0.17}Ga_{0.83}N$ film

An SEM micrograph of an obliquely viewed cross-section of a crack in an $Al_{0.37}Ga_{0.63}N$ film is shown in Fig. 5. The majority of the cracks observed by SEM and XTEM terminated at the AlGaN / GaN interface with a few penetrating slightly into the GaN layer. Cracks were never observed to reach the sapphire substrate. The circle indicates a region where the film overgrew the crack. Overgrowth of cracks was common in the AlGaN films that we examined. AFM imaging of the AlGaN surface revealed that the steps at the points of overgrowth often spread continuously from one platelet to the neighboring one, bridging the crack

It has been postulated in previous work that the AlGaN/GaN films cracked during cooling from growth temperatures, because of the observation that cracks appeared to propagate upward from the film/substrate interface. However, our direct measurements of the stress indicate that the stress relief occurred during deposition, not during cooling from the growth temperature (which would induce a compressive growth stress). Additionally, it is apparent from SEM, XTEM, and AFM images that when deposition was continued past the critical thickness the AlGaN film partially overgrew the cracks, giving the false impression that the cracks did not propagate to the surface.

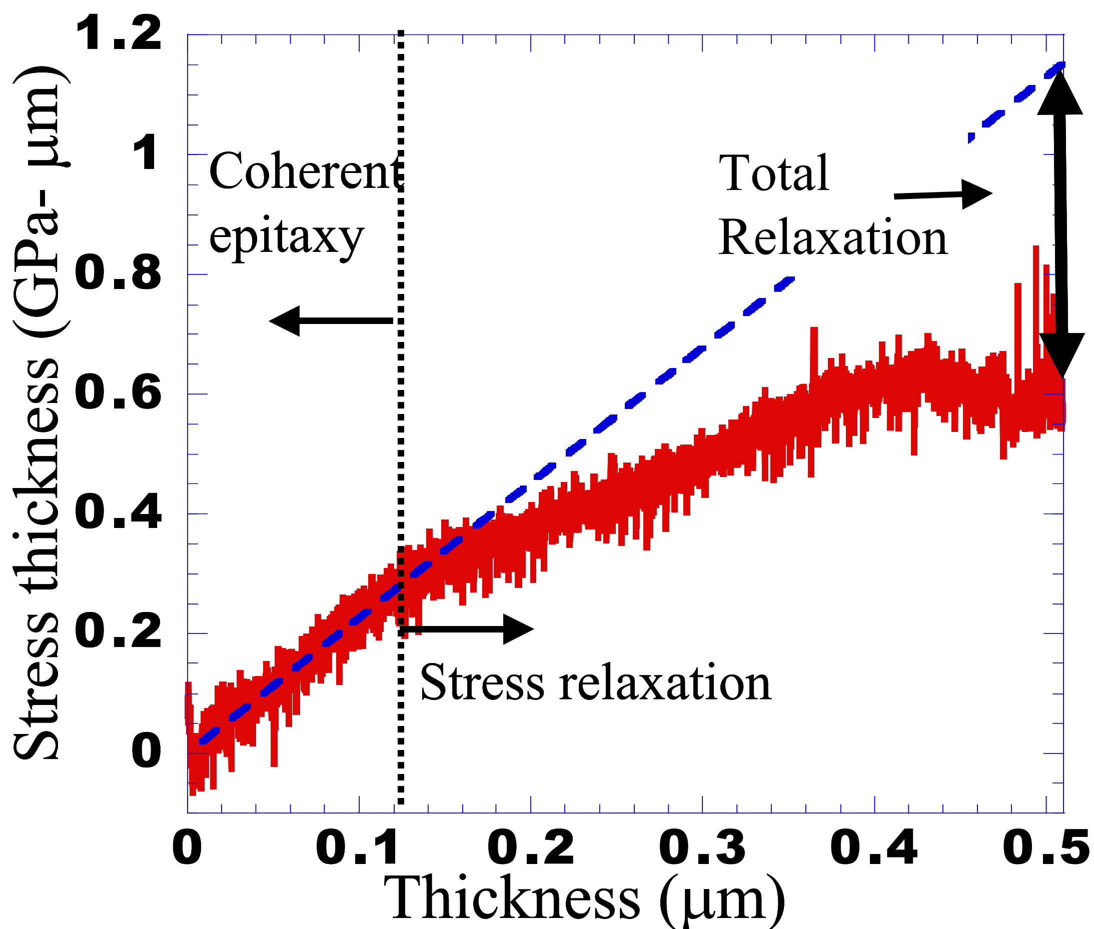

Figure 6. Stress-thickness plot of a 0.5μm $Al_{0.17}Ga_{0.83}N$ on 0.7μm of GaN film (not shown). The dot indicates the critical thickness

Fig. 6 shows the stress-thickness evolution during growth of an $Al_{0.17}Ga_{0.83}N$ film on HT GaN. The solid line is the stress-thickness measured by MOSS during deposition and the dashed line represent the estimated stress-thickness for fully coherent $Al_{0.17}Ga_{0.83}N$ film on the *strained* GaN film [8]. The coherency stress was estimated using the

aluminum concentration determined from *ex situ* XRD and the approximate $Al_{0.17}Ga_{0.83}N$ lattice parameter was calculated using a weighted average of the lattice constants of AlN and GaN at growth temperature [12]. The calculated coherency strain accounts for the initial stress up to the onset of stress relaxation using XRD. We have also verified by XRD that the films identified by MOSS to be fully coherent exhibited identical in-plane lattice parameters for AlGaN and GaN. Additionally, no misfit dislocations were observed at the AlGaN / GaN interface in XTEM images for these samples. The total relaxation in the film, equal to the difference in the expected coherence stress and the measured stress at the end of growth is also indicated on Fig. 6.

In all samples where stress relaxation was observed, the crack density did not account for the total stress reduction measured at the end of deposition using MOSS and XRD. The stress relaxation as a function of crack spacing can be estimated [13]:

$$\frac{\Delta\sigma}{\sigma_0} = \frac{1}{\zeta}\int_0^{\zeta}\left[\tanh(\beta\zeta)\sinh(\beta x) - \cosh(\beta x)\right]dx + 1\,, \tag{1}$$

where $\Delta\sigma$ is the stress relieved by the crack network, σ_0 is the initial coherency stress in the film, ζ is half the average crack spacing, and β is given by :

$$\beta \approx \sqrt{\frac{2G_f(1+\nu_f)}{h_f^2 M_f}}\,, \tag{2}$$

where ν_f is the Poisson ratio of the film, M_f is the film biaxial modulus for AlGaN, and G_f is the shear modulus of the film in the (0001) plane [14-16]. For the film in Fig. 6 the stress relief estimated from the crack network was 13%, which is well below the measured relaxation of 51%. This implies that additional stress relieving defects must also be present.

Fig. 7 is a XTEM image of the film in Fig. 5. A dense array of dislocations is visible at the AlGaN / GaN interface. The diffraction contrast of these dislocations indicate that their Burgers vectors have an edge component in the basal plane, which is consistent with their being strain relieving misfits. The mean spacing of the interfacial dislocations was ~50nm, which corresponds to a strain relief of 0.00424 or about ~70% of the total measured relaxation. The estimated stress relief from the crack network in this sample was ~30% of the measured relaxation, which is in reasonable agreement.

Our observation of combined brittle-ductile relaxation raises the question of whether the cracks or misfit dislocations are introduced first. Generally, the *equilibrium* critical thickness for dislocation introduction is smaller than that for cracking [17]. However, in the (0001)-oriented III-nitrides, effective slip systems for misfit dislocations are not readily available in planar films for the following reasons: (1) zero resolved shear stress on some slip systems; (2) other active slip systems do not result in interfacial

dislocations with an in-plane edge component; and (3) large kinetic barriers to glide may be present on higher order slip systems [18]. Thus we tentatively ascribe the observed critical thickness to be associated only with fracture. We further suggest that at least locally, the shear stress concentration surrounding crack tips at the AlGaN/GaN interface enhances both nucleation of misfit dislocations, and their subsequent glide. A possible slip system for relaxation is **b** = **a** dislocations gliding on the (0001) interfacial plane. A similar effect has been proposed by Jahnen *et al* [18] for the initiation of misfit dislocations at pinholes in compressively strained InGaN on GaN.

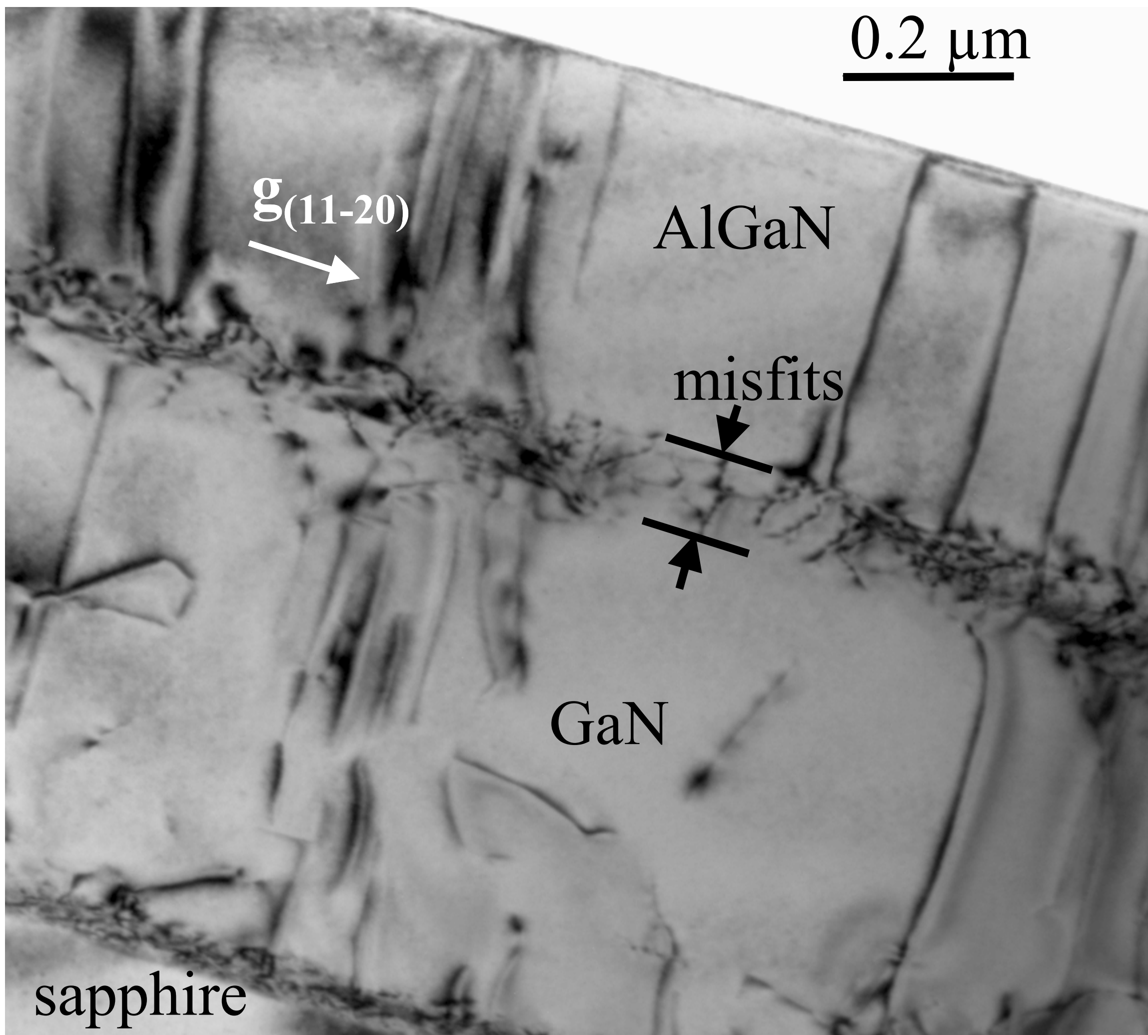

Figure 7. Bright-field XTEM image of dislocations in $Al_{0.37}Ga_{0.63}N$/GaN, using two-beam diffraction conditions with **g** = (11-20); [1-100] specimen tilted 30° about [11-20] axis to broaden the projected image of the interface.

The energetics of brittle failure may be described using the Griffith crack propagation criterion. In this expression the work required to create a new surface is balanced against the potential energy available in the form of internal stress in the film. A general expression for the critical thickness for crack propagation is given by [19]:

$$h_c = \frac{\Gamma M_f}{(1+\nu_f) Z \sigma_o^{\,2}} \tag{3}$$

where Z is a dimensionless crack driving force and Γ is the fracture resistance. We assume here that initially the fracture resistance is only associated with creation of new surface, and that there is no additional plastic deformation. Therefore, $\Gamma = 2\gamma_{(hklm)}$, where $\gamma_{(hklm)}$ is the surface energy of the crack plane. This does not exclude the possibility of plastic deformation during later stages of the growth. Z depends on the structure of the crack network and the ratio of biaxial moduli of the film and substrate, AlGaN and GaN in this case. For a "channel crack" pattern, such as we observed, with vertical cracks that terminate at the film/substrate interface, Z=1.975 [19].

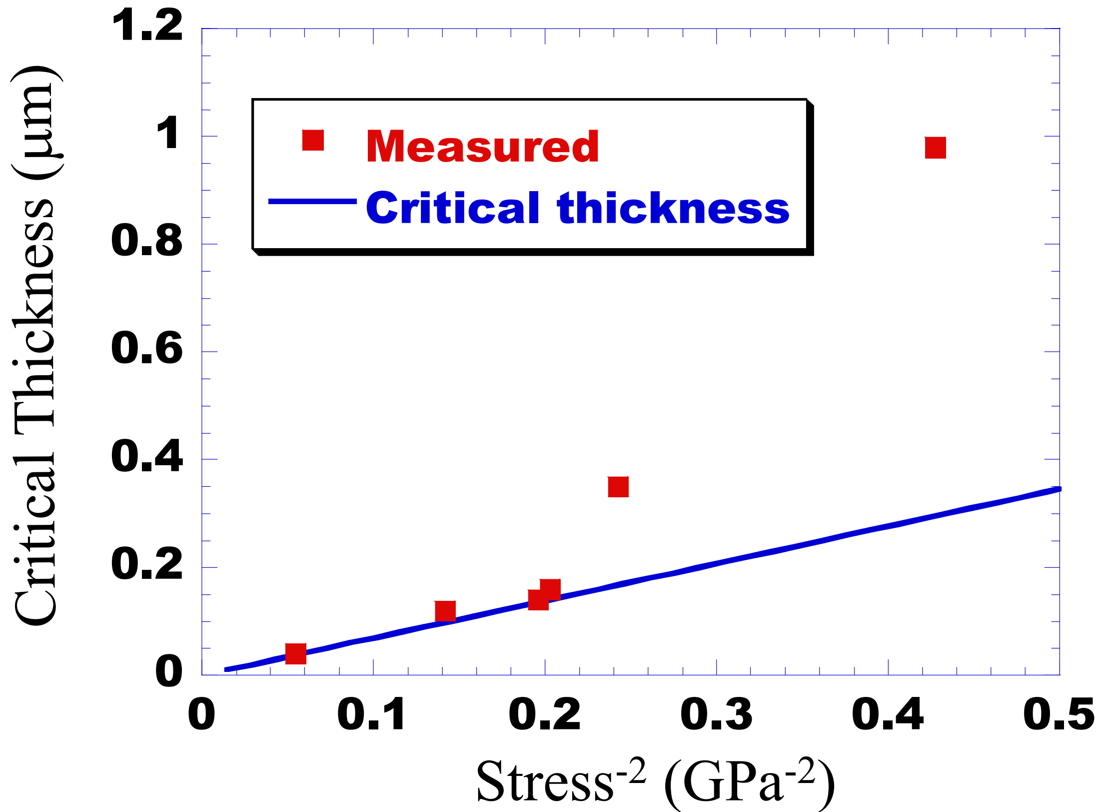

Figure 8. Plot of critical thickness versus $1/\sigma^2$ for six samples (squares). The line is the fracture critical thickness (eq. 3) using the Northup surface-energy values.

Fig. 8 is a compilation of the onsets of relaxation measured for six different samples. The line in the figure represents the equilibrium critical thickness determined from Eq. (3), where we used $\gamma_{\{11\underline{2}0\}} = 1.97$ J/m^2, from *ab initio* calculation by Northrup *et al* [18]. For any point above the line it is energetically favorable for a crack to propagate in the film, and below the line an existing crack can not propagate. We observe that four of the six samples failed near the calculated equilibrium critical thickness for cracking. This is consistent with the initial relaxation being due to propagation of cracks, which in turn activates slip systems for misfit dislocations. Note that the two lowest aluminum concentration samples grew considerably beyond the critical thickness, indicating that there were few incipient cracks or flaws to nucleate cracks.

We have directly measured the evolution of the growth stress during deposition of AlGaN on GaN, and showed that a brittle-ductile relaxation mechanism occurs. Misfit dislocations are created during the fracture process accounting for the majority of the stress relieved. The importance of fracture is that it permits activation of slip that was unable to occur in the initially planar films. We measure a critical thickness boundary that is consistent with channel cracks and a fracture resistance dominated only by the surface energy.

(This page intentionally left blank.)

The Effects of Biaxial Strain and Chemical Ordering on the Band Bap of InGaN

Wurtzite $In_xGa_{1-x}N$ has a direct band gap that can potentially be varied from 3.42 (x = 0) to 1.89 eV (x = 1), making it useful for fabricating blue and green light-emitting diodes. Recent experimental studies provided valuable insights into the properties of this alloy system [20-22], and two noteworthy observations have emerged from these studies: 1) Layers up to 2500 Å thick can be grown coherently on GaN in spite of the sizeable lattice mismatch (2.7% at $x = 0.25$, for example), and 2) The photoluminescence (PL) peak is often observed at a lower energy than the absorption edge, typically used to define the alloy band gap. Cubic (zinc-blende) $In_xGa_{1-x}N$ films have also been grown recently and their properties are somewhat different from those of wurtzite $In_xGa_{1-x}N$ (see below) [23,24]. Chichibu *et al*. [25] proposed that the PL redshift observed in wurtzite InGaN arises from the recombination of excitons localized in indium-rich regions, and this view has recently been extended by O'Donnell *et al.* [26] who speculated that quantum dots exist within the alloy matrix having compositions approaching InN. Phase separation and indium-rich regions are expected to occur in InGaN based on calculations using a modified valence force-field approach which predict a large region of solid-phase immiscibility [27]. Coherent growth of wurtzite InGaN results in compressive biaxial strain in the (0001) plane which can change the alloy band structure, and may also generate an internal electric field causing field-induced tail states to appear below the absorption edge via the Franz-Keldysh effect. [28]. Wetzel *et al.* [28] proposed that the PL redshift in strained alloys originates from these tail states, thereby providing an explanation that does not require the presence of composition fluctuations or quantum dots. We note that the zinc-blende InGaN films referred to above were grown unstrained on cubic substrates, so their optical properties were not affected by internal electric fields.

Notwithstanding the different proposed explanations for the PL redshift in wurtzite InGaN, alloy band gaps as measured by absorption-related techniques (absorption, photoreflectance and spectroscopic ellipsometry) vary significantly between samples grown by different groups. This is illustrated in Fig. 9 where we plot the gap deviations, $\Delta E_g = E_{g,InGaN} - xE_{g,InN} - (1-x)E_{g,GaN}$, from five sets of wurtzite and zinc-blende InGaN samples, where $E_{g,GaN}$ is the gap of GaN, $E_{g,InN}$ is the gap of InN, and $E_{g,InGaN}$ is the gap of InGaN. (The gap deviation is used here in order to emphasize the band-gap bowing and to facilitate comparisons between theory and measurements, and wurtzite and zinc-blende results. Also, due to the PL redshift mentioned above we only consider band gaps obtained using absorption-related techniques.) We note that gap deviations for the strained wurtzite films fall consistently below the values for unstrained zinc-blende films. This is surprising because biaxial strain in the wurtzite (0001) plane is predicted to increase band gaps in the constituent compounds [29]. One goal of this study was therefore to examine the effect of biaxial strain in wurtzite $In_xGa_{1-x}N$ films, and determine whether it could account for the larger-magnitude gap deviations seen in wurtzite alloys. We have also examined the effect of chemical ordering on the band gaps of strained wurtzite InGaN. This work was motivated by experimental studies showing evidence of cation ordering along the [0001]

direction in wurtzite alloys [30]. Furthermore, a recent theoretical study by Northrup *et al.* [31] reported that indium atoms have a 0.5 eV bias to incorporate at one of the two possible sites at a step edge in wurtzite InGaN, thereby providing a mechanism for ordering along the [0001] direction. We note that this mechanism does not apply to cubic structures, so the corresponding ordering (along the [111] direction) should not occur in zinc-blende InGaN.

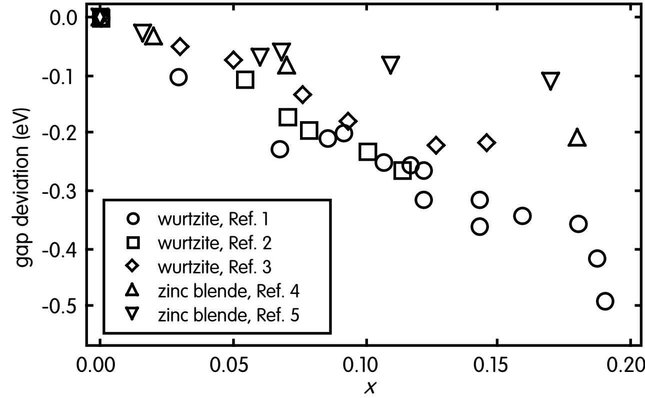

Figure 9. Measured gap deviations for strained wurtzite and unstrained zinc-blende InGaN. The gap deviations are computed using measured band gaps for unstrained wurtzite and zinc-blende GaN from the corresponding references, and assuming band gaps of 1.89 eV for wurtzite InN and 1.80 eV for zinc-blende InN.

Our calculations were performed using the Kohn-Sham formulation of density-functional theory within the local-density approximation (DFT-LDA) [32] with 192-atom supercells consisting of 4×4×3 primitive wurtzite cells. We considered the set of x values 0.0625, 0.125, 0.1875, 0.250, 0.375, and 0.5, and for each x we generated five distinct atomic configurations in order to assess the variation in computed alloy properties with configuration. Ordered configurations were generated by constraining indium atoms to reside on alternating planes along the [0001] direction and randomly occupying the cation sites within each plane consistent with the alloy composition. Non-ordered (random) configurations were generated by randomly occupying cation sites with indium atoms consistent with the alloy composition. Atom positions were fully relaxed for all of the supercells considered, and the cell shapes for unstrained cells were adjusted until the diagonal elements of the stress tensor were equal to zero. For strained cells, the lattice constant in the (0001) plane was fixed at the theoretical value for GaN, and the lattice constant perpendicular to this plane was adjusted until the corresponding component of the stress tensor was equal to zero. The calculations were performed using the plane-wave, ultrasoft pseudopotential formulation [33], employing pseudopotentials developed by Grossner *et al* [34]. The Brillouin zone was sampled using the Γ-point, and tests using Monkhorst-Pack [35] parameters {2,2,2} verified the adequacy of this sampling. For theoretical zinc-blende InGaN results and further discussions related to using DFT-LDA for alloy calculations, we refer to our earlier publication [36,37].

We first briefly discuss results related to wurtzite alloy lattice constants and stress-strain properties. The *a* lattice constants of the unstrained alloys were found to be within 0.4% of the composition-weighted averages of the constituent values and the *c* lattice constants were within 0.3%, indicating that Vegard's law [38] is valid for wurtzite InGaN. The *c* lattice constants of the random strained alloys were within 0.2% of the values predicted using composition-weighted lattice and elastic constants [39], indicating that no unusual behavior exists in terms of the mechanical response of InGaN to biaxial strain. Negligible differences in the strain along the *c*-axis strain were found between ordered and random structures.

In Fig. 10, we present our results for random unstrained wurtzite alloys. For each composition we show the average of the band gaps from the five configurations and the standard deviation. The band gap dependence on composition is nearly parabolic with bowing parameter, b, ranging from 1.2 ($x = 0.5$) to 1.5 eV ($x = 0.1875$) where the bowing parameter is defined in terms of the expression $\Delta E_g = -bx(1 - x)$. Our results in Fig. 10 are compared with measurements on unstrained zinc-blende InGaN and our previous theoretical results for zinc-blende InGaN [36]. The calculated wurtzite and zinc-blende gap deviations are in good agreement, providing confidence in the often made assumption that nitride alloys having these two structures should have similar band-gap bowing. The theoretical results are in good agreement with measurements by Goldhahn *et al*. [23], but are in rather poor agreement with the results of Brandt *et al*. [24] beyond $x = 0.1$.

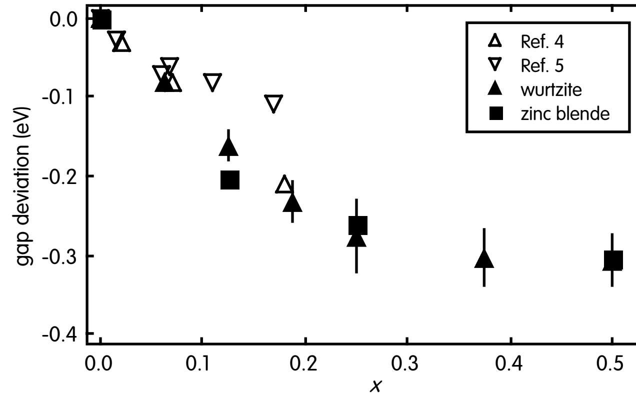

Figure 10. Calculated gap deviations for random unstrained wurtzite InGaN, estimated gap deviations for zinc-blende InGaN, and corresponding experimental results for zinc-blende InGaN. The symbols for the wurtzite results show the average of the gaps from the five configurations and the vertical lines give the standard deviations.

In Fig. 11, we display all of our results for wurtzite alloys. Straining the random alloy to be coherent with GaN increased the band gaps for $x < 0.25$ (decreasing the magnitude of the gap deviations) and decreased them for $x > 0.25$ (increasing the magnitude of the gap deviations). A similar nonlinear behavior was found for wurtzite

GaN under biaxial strain in the (0001) plane over the range $-0.04 \leq \varepsilon_{\|} \leq +0.01$ where $\varepsilon_{\|}$ is the in-plane strain parameter. Zinc-blende GaN displayed similar nonlinear behavior under biaxial strain in the (111) plane, but only weakly nonlinear behavior for biaxial strain in the (001) plane over the same range of strain parameters. As a check that these results were not an artifact of the pseudopotential approximation, we repeated the calculations using the all-electron, full-potential, linear muffin-tin orbitals method. Almost exact agreement was found both in the absolute values of the band gaps and their strain dependence. We also performed GW calculations [40] for the strain dependence of wurtzite GaN, and the results were very close to those obtained using DFT-LDA.

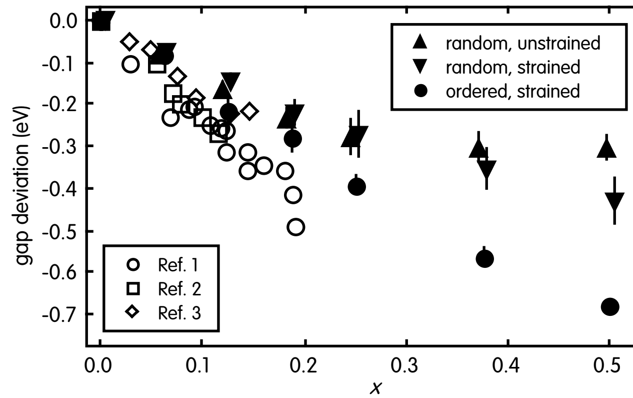

Figure 11. Calculated and experimental gap deviations for wurtzite. The symbols for the wurtzite results show the average of the gaps from the five configurations and the vertical lines give the standard deviations. Note that we have offset the compositions for the random results by ± 0.003 to make them easier to distinguish.

Ordering the strained alloys reduced their band gaps considerably as shown in Fig. 11. Before comparing these results to measurements, we note that the strain-induced electric field discussed by Wetzel *et al.* [28] can alter the alloy band structure aside from causing field-induced tail states. To estimate the magnitude of this effect, we note that the field will exert a force on an atom proportional to its ionic charge. If we assume a charge of −1 for nitrogen ions, +1 for cations, and a field strength of 1 MeV/cm, then the force on an atom will be 0.01 eV/Å in magnitude. These forces will lengthen the cation-nitrogen bond oriented along the *c*-axis and, as a secondary effect, change the *c* lattice constant. We estimated the field effect on the band gap by displacing the atoms in an $x = 0.5$ ordered alloy and relaxing the *c*-axis in response to these displacements. The resulting change in the alloy gap was +25 meV, which has little bearing on the comparisons or discussion presented below and we therefore neglect it.

Our strained wurtzite results are compared with corresponding measurements in Fig. 11. The results for random alloys fall above the measurements and are in poor agreement with them except for the results of Wagner *et al* [22]. Our strained wurtzite results are compared with corresponding measurements in Fig. 11. The results for random alloys fall above the measurements and are in poor agreement with them except for the

results of Wagner *et al.* [20] and McCluskey *et al.* [21] remain substantial. In addition, we note that O'Donnell *et al.* [41] estimated a gap deviation of ΔE_g = -1.45x eV for $In_xGa_{1-x}N$ in the range $0 \leq x \leq 0.4$. A linear fit to our strained, ordered results yields ΔE_g = -1.5x eV in excellent agreement with their estimate. O'Donnell *et al.* [41] also remarked that their measurements showed a linear form (or lack of a parabolic form) for the gap deviations. Our calculations indicate that this behavior arises mainly from the nonlinear response of the alloy gap to biaxial strain, although ordering also enhances the linearity beyond x = 0.25.

In summary, our results for random unstrained wurtzite alloys and our previous estimates for zinc-blende alloys are in good agreement with each other, and with the measurements on unstrained zinc-blende InGaN by Goldhahn *et al* [23]. However, our zinc-blende results and those of Goldhahn *et al*. [23] do not agree well with the measurements of Brandt *et al*. [24] which display smaller-magnitude gap deviations. Further experimental studies would be helpful in establishing the proper band-gap dependence on composition for zinc-blende InGaN. In this regard, however, we point out that the discrepancies in the zinc-blende measurements are only slightly larger than among measurements on wurtzite alloys where there is presumably more overall growth experience. We also note that the level of agreement obtained herein with zinc-blende measurements was not achieved in two recent theoretical studies on zinc-blende InGaN [42] which displayed significantly larger-magnitude gap deviations. Our results indicate that biaxial strain by itself cannot account for the noticeable differences in measured gap deviations between wurtzite and zinc-blende alloys. However, we do find an interesting, nonlinear band-gap dependence on strain, both for InGaN and for several bulk III-V compounds. Ordering along the [0001] direction is found to reduce the band gaps of strained wurtzite alloys considerably, producing good agreement with the measurements of Wagner *et al*. [22] and O'Donnell *et al* [41]. However, discrepancies with the measurements of Wetzel *et al*. [20] and McCluskey *et al*. [21] remain substantial. While ordering does not reconcile theoretical predictions with all of the available measurements, it nevertheless seems worthwhile to look for evidence of ordering in a broader set of samples than has been examined up to now. Further studies aimed at resolving the differences among wurtzite measurements would likewise be worthwhile, and studies aimed at understanding composition fluctuations or quantum-dot formation in this alloy system would be particularly useful.

(This page intentionally left blank.)

MOCVD Growth of Quaternary (Al,Ga,In)N for UV Optoelectronics

Preliminary work in the AlGaN/GaN quantum well (QW) UV emitters [43] suggested that the use of a binary GaN active region results in a low optical output power. Furthermore, mismatch-induced tensile stress was observed during growth of AlGaN heterostructures on thick GaN templates for UV devices [44], leading to relaxation through crack generation. Quaternary AlGaInN compound semiconductors are expected to enclose a finite (non-zero) area on the plot of energy gap versus lattice constant. In principle the employment of quaternary compounds should render flexibility in tailoring bandgap profile while maintaining lattice matching and structural integrity. In this work we summarize our investigation on the issues of optical efficiency and strain control using quaternary AlGaInN compound.

The MOVPE growth was carried out in a vertical rotating-disc reactor. All of the quaternary epilayers and multiple quantum well (MQW) structures were grown on 1-µm GaN epilayers at 1050°C using a standard two-step nucleation procedure (on sapphire) with low-temperature GaN grown at 550 °C [45]. The growth temperature of the quaternary AlGaInN was varied between 750 and 820 °C. The reactor pressure was held constant at 200 Torr. The NH_3 and N_2 flows were set at 6 *l*/min each. An additional flow of H_2 (~400 cm^3/min) was employed as a carrier gas. Trimethylgallium, triethylaluminum, and trimethylindium were employed as metalorganic precursors.

Given the scarcity of reliable information concerning the quaternary, it is imperative to accurately determine the concentrations of the constituent elements. Concentrations of In and Al in the films were measured using Rutherford backscattering spectrometry (RBS) [46] with a 2.5 MeV $^4He^+$ ion beam. Ion-channeling effects in the RBS spectra were randomized by tilting the sample 10° from normal to the analysis beam and continuously rotating the sample about its normal during the analysis. Al and In concentrations were then extracted from the spectra using the SIMNRA (ver. 4.4) simulation program [47]. Figure 12 shows a representative RBS spectrum from AlGaInN. The solid line is the fitted simulation, while the dashed line is a simulation for the same In concentration with no Al. The inset shows a diagram of the measured film on GaN, along with the fitted concentration values for In and Al. The large backscattering yield from In, coupled with the accurately known nuclear cross section, results in a relatively high accuracy for the determination of the In concentration. We estimate an uncertainty of ±0.002 at an In concentration of 0.01, and ±0.005 for a concentration of 0.10. Because the backscattering yield from Al is much smaller, the Al concentration was determined less directly by measuring a reduction, or dip, in the yield from Ga, due to the presence of the Al and In in the layer. An uncertainty of ±0.01 at an Al concentration of 0.10, and ±0.02 for a concentration of 0.20 was estimated for the cited data.

A high-resolution triple-axis x-ray diffractometer (Philips X'Pert System) was employed to assess the structural quality and determine both in-plane (***a***) and out-of-plane (***c***) lattice parameters using symmetric (0002) and asymmetric (202-4) (using grazing-

incidence) diffractions. Photoluminescence (PL) was measured using a HeCd laser (325 nm) as the excitation source in conjunction with a 0.3 meter spectrometer and a UV enhanced CCD detector. Typical excitation level is around 30 W/cm^2. Real time wafer curvature measurements were performed with a multi-beam optical stress sensor (MOSS) [48] modified for use on our reactor. To determine the wafer curvature, the divergence of an array of initially parallel laser beams is measured on a CCD camera after reflection of the array from the film/substrate surface. Changes in wafer curvature induce a proportional change in the beam spacing on the camera. This technique provides a direct measurement of the stress-thickness product during MOVPE of GaN [49].

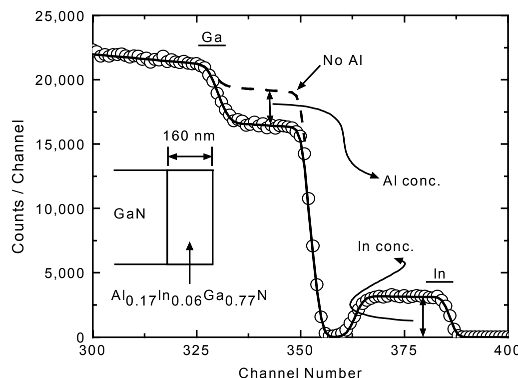

Figure 12. An RBS spectrum from an AlGaInN sample. The solid line is a simulated fit.

In attempting to extract band gap energy from a PL measurement for the AlGaInN quaternary system, one is reminded that the determination of band gap energy for GaInN has been a subject of much debate [50]. Indium-related compositional fluctuation is expected to contribute to a Stokes-like shift with a magnitude of less than 100 meV [51]. Field-induced separation of electrons and holes (due to piezo- and spontaneous polarization) causes a red shift (up to 300 meV) of PL emission energy in quantum well structures [52] but should not be of significance in epilayers thicker than 50 nm. Finally, the existence of a compressive or tensile biaxial strain, due to a combination of lattice mismatch [53] and thermal mismatch, introduces a blue or red shift, respectively, to the band gap energy as determined by the deformation potentials [54]. Given that the In fraction is limited to 10% and the pseudomorphic strain in the quaternary does not exceed 1% in compression, we estimate (using published deformation potentials [55]) that the difference between PL emission energy and band gap to be less than 100 meV in the epilayers reported here.

In our earlier work we have shown an AlGaN/GaN QW LED emitting at a wavelength of 354 nm [43]. The power output of the prototype UV emitter was around 13 μW at a current level of 20 mA, which is about 3 orders of magnitude lower than the commercial high-brightness blue LEDs. A series of test samples, consisted of 0.5 μm of GaN test layers grown on a standard GaN epilayer (of 1 μm thick), were grown to optimize

the optical quality of the active region. Photoluminescence (PL) at room temperature (RT) was employed to measure the optical quality. Among the growth parameters investigated, reactor pressure was found to have a distinct effect on the PL emission intensity. As the growth pressure was increased from 80 Torr (the pressure employed in the previous LEDs and chosen to mitigate the gas-phase reaction during growth of AlGaN) to 250 Torr, integrated PL intensity increased by more than 10 times and peaked at around 200 Torr. The mechanism responsible for the observed enhancement of GaN emission is not known. One might speculate that a reduction of carbon incorporation, due to an increase of the partial pressures of both NH_3 and H_2, reduces the non-radiative recombination paths [56].

Recently it has been reported by several groups [57-59] that the addition of a small amount of indium could lead to an enhancement in PL emission efficiency. Mukai et al. [57] demonstrated an GaN:In UV LED with an indium content of around 2% and optical power output as high as 5 mW. A series of GaN:In samples (0.2 μm thick on 1 μm GaN epilayers) were grown in which the indium fraction was increased from 0 to approximately 4% as determined by x-ray and RBS. Figure 13 shows the PL spectrum of the GaN:In layers with the spectrum from an "optimized" GaN layer as a reference (the bottom trace peaking at 364 nm). At the expense of a shift of emission peak toward longer wavelengths (~380 nm), we attained an increase of more than one order of magnitude in integrated light intensity. Two explanations have been offered to explain the observed enhancement in light emission: carrier localization due to indium incorporation [57] or the suppression of non-radiative recombination defects in the presence of indium [58]. Discussions of these mechanisms are presented in another chapter.

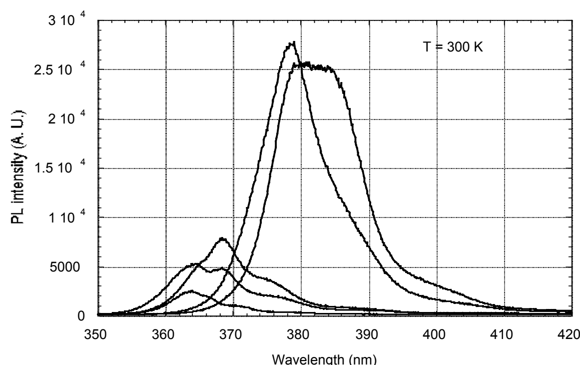

Figure 13. PL of GaInN epilayers with various amount of Indium. The integrated intensity increases by more than 10 times from GaN to 4% GaInN.

Only limited information has been published concerning the AlGaInN quaternary system. Matsuoka [60] predicted the presence of an unstable mixing region (spinodal phase separation) in wurtzite AlGaInN as the indium content increases. The challenges associated with the growth of AlGaInN, primarily the selection of conditions necessary to enable

surface diffusion of Al and Ga species while at the same time preventing the surface re-evaporation of In, are partially manifested by the scarcity of experimental data. McIntosh *et al*. [61] and Yamaguchi *et al.* [62] reported the physical incorporation of Al and In into GaN by MOVPE. Aiming at proof-of-concept demonstrations of material synthesis, little information was provided in either work concerning the bandgap versus alloy compositions. The functional feasibility of AlGaInN as a confinement barrier also remained ambiguous in these studies since PL emission (energies) from samples investigated did not exceed the emission (energy) of GaN (~363 nm/ 3.42 eV)). The concern was reiterated by Peng *et al*. [63] in stating, based on optical absorption measurements of sputtered polycrystalline films, that AlInN and AlGaInN do not seem to provide good confinement (to GaInN) due to a very strong bowing effect. We have shown from in-situ stress measurement that the use of high Al-fraction (or thick) AlGaN barriers on GaN templates, required for electrical and optical confinement in UV devices, leads to a buildup of tensile stress and subsequently the occurrence of cracking [44]. As discussed in this section, introducing indium into GaN greatly enhances the optical efficiency but at the cost of an increase in emission wavelength. Investigation of quaternary AlGaInN was initiated by the two constraints encountered in the use of ternaries AlGaN and GaInN as barriers and wells, respectively. It is expected that AlGaInN would render flexibility in controlling the mismatch strain and bandgap profile.

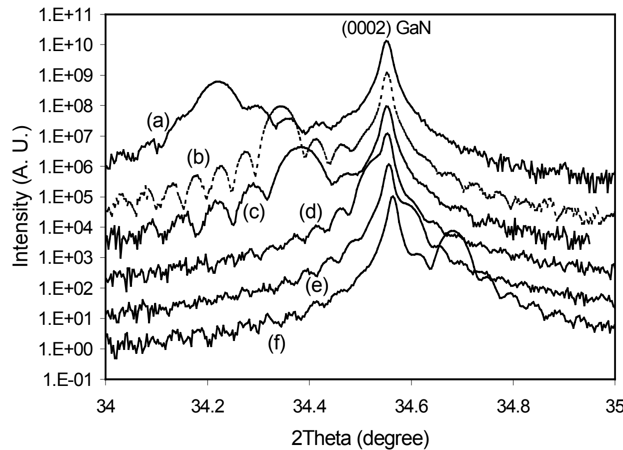

Figure 14. (0002) 2θ-ω x-ray diffraction of AlGaInN (solid traces) and GaInN (dashed line) epilayers showing a range of lattice parameters bracketing

Figure 14 shows (0002) 2θ−ω x-ray diffraction (XRD) scans (with an analyzer-crystal detector) for several AlGaInN (a, c-f) and GaInN (b) epilayer samples. Thickness of the samples varies from 0.14 to 0.20 μm, as indicated by the change of the period of the diffraction fringes. (Thin film thickness derived independently from x-ray fringes and from RBS simulations differed by less than 5% in most cases.) By adjusting the relative Al and In compositions, one observes a change of the out-of-plane lattice parameter from being larger (top trace) to smaller (bottom trace) than that of GaN. Pseudomorphic growth is verified by measuring the in-plane lattice parameter (***a***) of the epilayers. Unlike the case

in zincblende semiconductor heterostructure, the appearance of an overlap between the (0002) diffraction peak from the quaternary and the peak from GaN (a condition between scans (d) and (e)) does not necessarily imply a lattice-matched strain-free epitaxy as the in-plane and out-of-plane lattice parameters of AlN, GaN, and InN do not vary in a linear manner. Using the published lattice parameters [53], exact match of the ***a*** lattice constant of AlInN to GaN should occur at an Al fraction of 18% while it takes approximately 28% Al in AlInN to match the out-of-plane (***c***) lattice parameter of GaN. A quaternary compound with a ***c*** lattice parameter matched to GaN is speculated to be under biaxial compression during growth.

Optical properties of the AlGaInN samples (d and f in Figure 14) were investigated with RT PL (Figure 15). The PL from a "standard" GaN epilayer was included for comparison. It is clear from Figure 15 that the AlGaInN epilayer emits with energy higher than that of GaN. The $Al_{0.14}Ga_{0.82}In_{0.04}N$ epilayer (sample (d) in Figures 14 and 15) gives the indication that one can synthesize a wider bandgap (than GaN) quaternary AlGaInN compound yet with an in-plane lattice constant *larger* than that of GaN. It is worth noting that the integrated PL intensity from this quaternary is about three times brighter than that from GaN. There has been much empirical observation and speculation that the presence of indium in GaInN ternary layers seems to preserve excited carriers from recombining at non-radiative centers [64]. Mukai *et al*. [57] reported, in the development of ultra-violet LEDs, a rapid reduction of optical efficiency as the In content in the GaInN active region decreased below a certain value. The implication is that the carrier-localization effect [64], possibly due to the presence of a compositional fluctuation of indium, could make AlGaInN an alternative (to GaN or AlGaN) as a short-wavelength (λ<360nm) light-emitting medium.

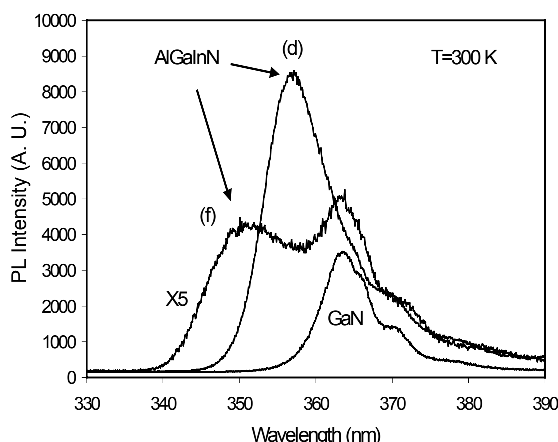

Figure 15. Room-temperature photoluminescence from a GaN (solid line) epilayer and two AlGaInN epilayers (samples d and f).

For the design and implementation of quaternary heterostructure devices, it is helpful to superimpose contours of constant lattice parameter and "bandgap" (or more

precisely, PL peak) energy as functions of the alloy compositions. A series of AlGaInN, GaInN, and AlGaN epilayers have been grown and the characterizations are summarized in Figure 16. $Al_yGa_{1-x-y}In_xN$ is described in this work by a right-angle triangle with AlGaN and GaInN forming the two sides around the right-angle vortex. (The hypotenuse corresponds to the ternary AlInN, not shown in Figure 16.) The location of any $Al_yGa_{1-x-y}In_xN$ quaternary is uniquely specified by the In (x) and Al (y). The triangles, diamonds, and circles represent the data points for AlGaN, GaInN, and AlGaInN, respectively. The compositions of the ternaries were determined primarily by x-ray diffraction and independently confirmed by RBS, the quaternary compositions were determined by RBS. The solid line with a slope of around 4.4 defines the quaternary alloys that are lattice matched to GaN; one can construct an array of parallel lines for lattice-matched growth with different in-plane lattice parameters. (Vegard's law predicts that the in-plane lattice parameter will remain unchanged when the increments of Al (ΔAl) and In (ΔIn) maintain a ratio of 4.44.) Quaternary alloys located to the lower right half of the straight line are expected to be under compression on a GaN template. The distance between a given data point on this plot and the solid line gives a qualitative measure of mismatch-induced strain.

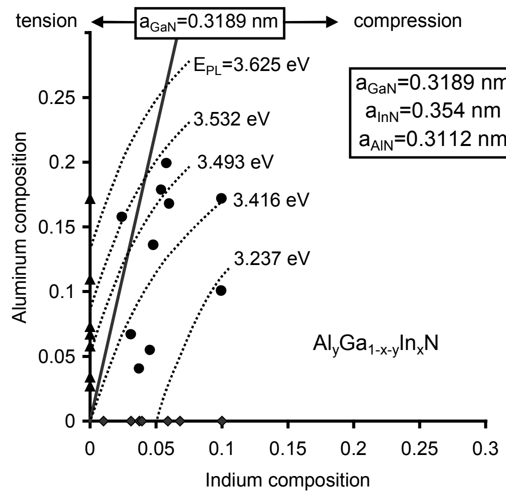

Figure 16. Contour plot of constant (in-plane) lattice parameter and emission energy versus Al and In compositions for AlGaInN epilayers.

PL investigation of the near band-edge emission is summarized by the dashed curves (denoting contours of constant PL peak energy) in Figure 16. The dashed contours are derived based on two assumptions: i) all the data points should be fitted by contours with nearly identical forms, and ii) the contours should be consistent with the available (theoretical [65] and experimental [66]) bowing information of ternary AlInN. Along each dashed line, the emission wavelength remains constant while the in-plane lattice parameter (and therefore strain) can be adjusted by varying the Al and In fractions. Since the In-related Stokes-shift tends to increase with an increasing In composition, the slopes of the contours for the actual bandgap energy might be less steep.

To demonstrate the possibility of heterostructures incorporating quaternary AlGaInN, we have grown multiple quantum well (MQW) structures consisting of 10 periods of AlGaInN barriers (Al~14%, In~4%, ~100Å) and GaInN wells (In~4%, ~45Å). Figure 17 shows the (0002) 2θ−ω XRD from the MQW structure. The presence of satellite peaks and other interference fringes is indicative of structural order and coherency (along the growth direction). Cross-sectional TEM images (Figure 18) indicated that the AlGaInN/GaInN interfaces are smooth and coherent on the atomic scale. One also notices from Figure 17 that the AlGaInN/GaInN MQW has a zero-order peak that corresponds to the lattice constant of a 2.0% GaInN alloy. In-situ stress/strain monitoring was conducted during the growth of a similar MQW structure and is shown in Figure 19. While the GaN layer is under tension [49] during growth (0.40 GPa), the AlGaInN/GaInN MQW region is under compression during growth (~0.47±0.07 GPa). Assuming a compressive thermal mismatch stress of 0.2 GPa from 1050°C to 800°C, one can estimate an average compressive mismatch strain of 0.15%, corresponding to the lattice constant of a 1.4% GaInN epilayer.

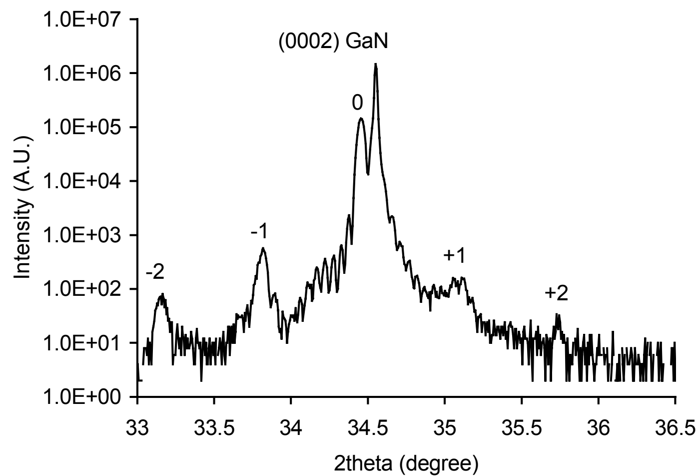

Figure 17. (0002) 2θ-ω x-ray diffraction of an AlGaInN (100Å)/GaInN (45Å) multiple (10) quantum wells

Optical quality of the AlGaInN/GaN MQWs was investigated using temperature-dependent PL. It is generally assumed that the non-radiative recombination mechanisms are thermally activated and the decay of integrated PL intensity from low temperature to room temperature renders a quantative measurement of the nonradiative processes [67,68]. Figure 20 shows the temperature-dependent PL with a plot of the integrated intensity in the inset. A reduction of 4.5 times of the integrated PL intensity from 4K to RT is comparable to the best reported for GaInN MQWs emitting at around 450 nm [69]. This also implies that an upper limit to the internal quantum efficiency of 20% is obtained at RT.

In summary, we report the MOVPE growth and characterization of quaternary AlGaInN. Contours of constant PL peak energy and lattice parameter of AlGaInN were

projected onto a two-dimensional plot. We confirmed that the employment of this novel quaternary compound could facilitate the tailoring of energy gap and lattice mismatch for design flexibility. In spite of the previous speculation that strong bowing could hinder the usage as a short-wavelength light emitter, we observed PL emission as short as 351 nm from a layer with about 20% Al and 5% In. The possibility of replacing AlGaN as an alternative barrier material was demonstrated through an AlGaInN/GaInN MQW structure.

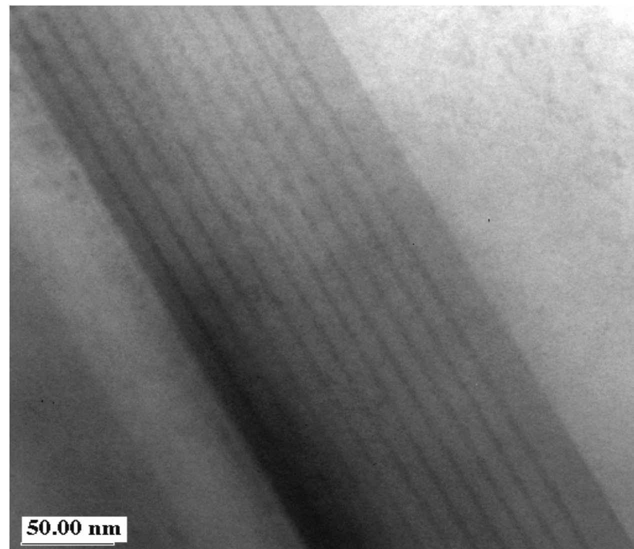

Figure 18. Cross-sectional TEM image of an AlGaInN (100Å)/GaInN (45Å) multiple (10) quantum wells.

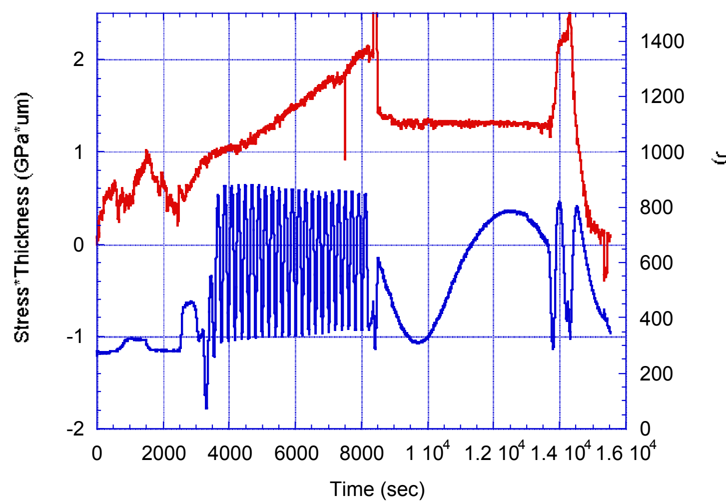

Figure 19. In-situ stress measurement of during growth of an MQW LED.

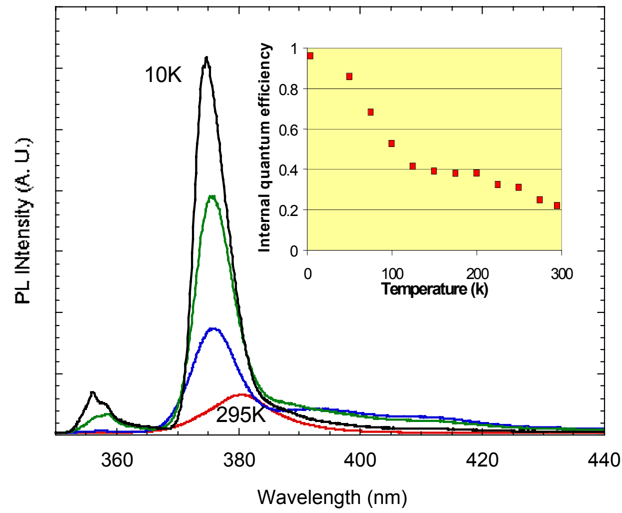

Figure 20. Temperature-dependent PL (at 10, 75, 150, and 295 K with decreasing ….. intensity) suggesting an internal quantum efficiency of around 20% from the AlGaInN/GaInN MQWs.

(This page intentionally left blank.)

Study of In-Containing UV LED Alloy Material

While much of the research in the nitride field has focused on the development of blue and green LEDs and laser diodes, UV ($\lambda < 400$ nm) LEDs based on GaN, AlGaN and/or AlGaInN active regions are also of great interest and are well suited to a number of applications. One of the most promising uses of a UV LED is as a high energy excitation source. In the biomedical and chemical sensing fields, UV LEDs can be used as compact and robust excitation sources of fluorescence. UV LEDs may also prove to be superior to blue LEDs in exciting phosphors for white lighting applications, due to improved color rendering. To date, there have been relatively few reports of UV LEDs based on the wide-bandgap nitride semiconductors. In particular, Akasaki et. al. [70] reported on a GaN/AlGaN double heterostructure (DH) LED with emission at 370 nm and up to 1.5% external quantum efficiency. Mukai, et. al. [71] have achieved an impressive 5 mW output at 371 nm from an InGaN/AlGaN DH LED with very low levels of indium (In) in the active region. That LED was reported to have up to 7.5% external quantum efficiency but the efficiency dropped by more than an order of magnitude as the emission wavelength shifted to 368 nm with the total elimination of In from the active region. Shorter wavelengths have been achieved by Han, et. al. [72] through a GaN/AlGaN multiquantum well (MQW) structure. These LEDs demonstrated a 354 nm emission peak with a narrow FWHM linewidth of 5.8 nm and relatively low output powers of 13 μW at 20 mA. Thus, while one group has demonstrated high (> 5%) efficiency LED performance for $\lambda > 370$ nm, many of the challenges inherent to the shorter wavelength emission regime still remain.

The nitride materials described in this work were grown in a high speed (~ 1200 rpm) rotating disk MOCVD reactor on two inch sapphire substrates. Different growth conditions were employed for non-indium containing alloys (GaN, AlGaN) as compared to indium containing alloys (InGaN, AlInGaN). The GaN and AlGaN growths were typically carried out at 1000-1080°C with hydrogen as the carrier gas. Ammonia (NH_3), Trimethylgallium (TMGa), Trimethylaluminum (TMAl) were used as the N, Ga, and Al precursors, respectively. The growth of InGaN and AlInGaN was carried out at 750-800°C, with nitrogen as the carrier gas and Triethylaluminum (TEA) and Trimethylindium (TMI) as the Al and In sources, respectively. A standard two-step growth (550 and 1050 °C for the low and high temperatures, respectively) with GaN low-temperature buffer layer (~250 Å) was used in this work.

We will focus on two general heterostructures for UV LEDs. The overall layer sequence is quite similar for the two structures, and is shown in Figure 21. The first design is an MQW LED structure with GaN quantum wells and $Al_xGa_{1-x}N$ barriers and emission in the $\lambda < 360$ nm region. The n-GaN buffer layer is typically 3 μm in thickness and Si-doped to a level of $2\text{-}5 \times 10^{18}$ cm^{-3}. The n-AlGaN cladding with x=0.15-0.20 is approximately 400 Å thick and doped to a similar level as the n-GaN layer. The multiquantum well region consists of 5 periods of 30 Å thick GaN quantum wells and 70 Å thick AlGaN (x=0.15-0.2) barriers. The p-AlGaN cladding is typically 400 Å thick and

the contact layer is 0.05-0.1 μm thick p-GaN. The second type of UV LED structure utilizes InGaN QWs and AlInGaN barriers in the MQW active region. The MQW region consists of 47 Å thick $In_xGa_{1-x}N$ quantum wells with x=0.04 and 48 Å thick $Al_yIn_xGa_{1-x-y}N$ barriers with x=0.04 and y=0.14. The p-GaN cap layer is thicker for these structures, due to the fact that the longer wavelengths emitted from the active regions are not as strongly absorbed by the p-GaN layer. Thicknesses of 0.1 μm to 0.25 μm have been used.

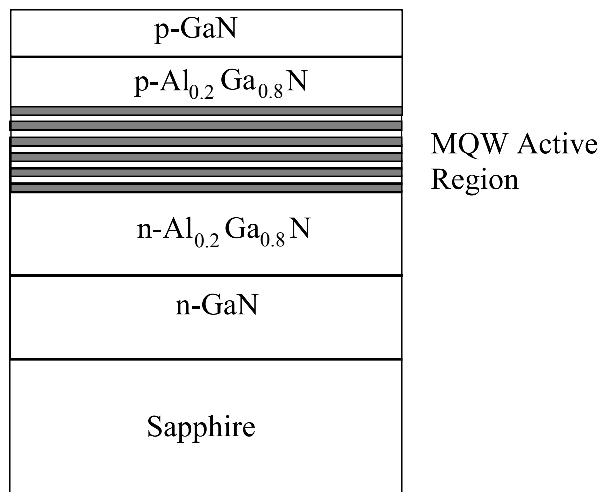

Figure 21. Schematic of UV LED MQW heterostructures.

One of the most intriguing issues in the nitride field concerns the high optical efficiency of nitride-based blue and green LEDs. Specifically, although a great deal of progress has been made in the development of InGaN-based light emitters, the role played by indium (In) in contributing to the optical efficiency is still quite controversial. A number of groups have proposed that the inhomogeneity of In incorporation results in carrier localization at In-rich regions and that this localization leads to enhanced optical efficiency [73-75]. Support of this hypothesis is found in cathodoluminescence experiments that demonstrate a variation of the PL emission energy on the microscale, suggesting that In composition variations on the order of several percent are possible [76]. Further insight is suggested by the time-resolved spectroscopy experiments of InGaN quantum well structures performed by Narukawa, et. al. [77], which suggest that the density of non-radiative centers and possibly the non-radiative recombination mechanism itself is altered when In is included in the growth. A similar result was obtained by Kumano, et. al. [78] who suggest that increased optical efficiency is due to reduced non-radiative recombination centers with In incorporation. Thus, it is clear that a strong consensus has not emerged as to how the presence of In in the QWs affects the optical efficiency and whether it is absolutely necessary for achieving high efficiency nitride LEDs.

This issue of whether In-containing QWs are needed for high efficiency is especially critical if we look at UV LED structures. Clearly the GaN MQW LEDs do not contain In in the active regions, and therefore would not benefit from the proposed improvements in optical efficiency seen in the blue and green LEDs. Furthermore, in order to achieve LED emission at $\lambda < 390$ nm from InGaN MQW structures, the In composition must be reduced to relatively small values ($x < 0.06$). Thus even in the InGaN/ AlInGaN MQW structures described in this report, the role played by In could be significantly reduced from that of blue and green LED structures with higher In compositions in the InGaN QWs.

In an effort to further elucidate these issues, we have performed a number of photoluminescence studies of InGaN, GaN and AlGaN MQW and bulk structures. In particular, we have performed temperature-dependent photoluminescence (PL) spectroscopy measurements on a number of MOVPE grown $In_xGa_{1-x}N$ epilayers in the low In composition regime ($x < 0.10$). This composition regime was chosen to examine whether a clear trend in optical efficiency and temperature dependent quenching of PL intensity can be found with the addition of just small amounts of In. Our work has also intentionally focused on relatively thick (0.2 μm) and doped bulk InGaN epilayers so that the role of piezoelectric field effects would be minimized [79]. This work is therefore distinct from the majority of the previously reported work that has focused on InGaN quantum wells with relatively high ($x \geq 0.2$) In composition.

The PL measurements were performed using a HeCd laser (325 nm) at a low power density of approximately 30 W/cm^2. A 0.3 meter spectrometer with an integrated UV enhanced CCD detector was used, with a spectral resolution of approximately 0.2 nm. The room temperature PL spectra for four InGaN epilayers is shown in Figure 22b. A strong increase in the integrated PL intensity is seen as In composition is increased, with more than a 25X increase as the peak wavelength shifts from 363-397 nm. The data suggest that the optical efficiency is highly dependent on the In composition. The full temperature dependence of the integrated PL intensity is plotted in an Arrhenius plot in Figure 22b. The data is fit with the following formula [80]

$$I=I_0/[1+\alpha \exp(-E_a/kT)]. \qquad (1)$$

Here the non-radiative decay is assumed to be thermally activated such that the non-radiative lifetime $\tau_{nr}=\tau_o \exp(E_a/kT)$ and E_a is the activation energy for PL quenching. The parameter α is equal to τ_r/τ_o where τ_r is the radiative lifetime. From the E_a values, we see a systematic increase in the activation energy as the indium composition is increased. The full temperature dependent data thus give further support of the hypothesis that increasing In composition improves the optical efficiency of the materials. Through the increasing E_a values with increasing In composition, we see that the In is reducing the effectiveness of non-radiative recombination mechanisms in quenching the PL intensity. Whether this effect is due to carrier localization or a modification of the nature of the non-radiative centers can not be determined from the data.

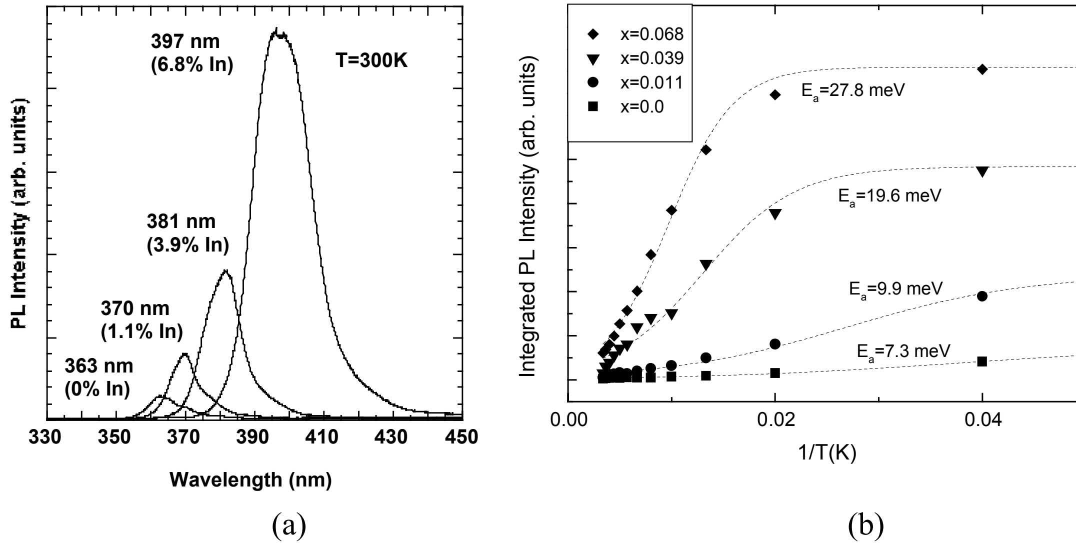

Figure 22. (a) Room temperature PL spectra of InGaN bulk epilayers and (b) Temperature dependent integrated PL intensity of InGaN bulk epilayers with In composition x. The E_a values are derived from fitting the data to equation 1.

Additional temperature dependent PL measurements were performed on InGaN, GaN and AlGaN MQW structures. The InGaN QW structures were supplied by Meijo University and have 10 periods of 23 Å thick $In_{0.21}GaN_{0.79}N$ QWs with GaN barriers. The GaN MQW structure was grown at Sandia National Laboratories and consists of 4 periods of 30 Å thick GaN quantum wells with $Al_{0.20}Ga_{0.80}N$ barriers. It should be noted that this GaN MQW structure was grown on an AlGaN buffer so that the QW emission would not be confused with emission from a thick GaN buffer layer. The AlGaN MQW structure was identical to the GaN MQW structure except that approximately 5% aluminum was added to the QWs. In Figure 23a, we show the low temperature (T=10K) photoluminescence spectra for the three MQW structures. In Figure 23b, we show the temperature dependence of the peak PL intensity for the three MQW structures. A strong distinction is seen in the total drop in peak PL intensity. In particular, the InGaN MQW structure experiences a relatively small (4X) loss in peak PL intensity from 10-300K, while the peak PL drop is 60X and 1000X for the GaN MQW and AlGaN MQW structure, respectively. In the quantitative comparison of the PL data for these three MQW structures, it is important to recognize that the growth conditions for the visible and UV MQW structures were quite different, and it is possible that further optimization of the growth conditions for the UV MQW structures would improve the performance. Nevertheless, this data is a good representation of the performance of our current GaN MQWs and high quality InGaN MQWs. In this data, we see evidence that the discrepancy in the optical efficiency between the visible and UV MQW structures is highly temperature dependent. In particular, the UV MQW structures are more susceptible to non-radiative recombination processes which serve to quench the PL intensities at room temperature. Furthermore, the severe 1000x drop in intensity from 10-300K for the AlGaN MQWs

suggests the increasing challenge of obtaining high optical efficiency at wavelengths in the 340 nm region and shorter.

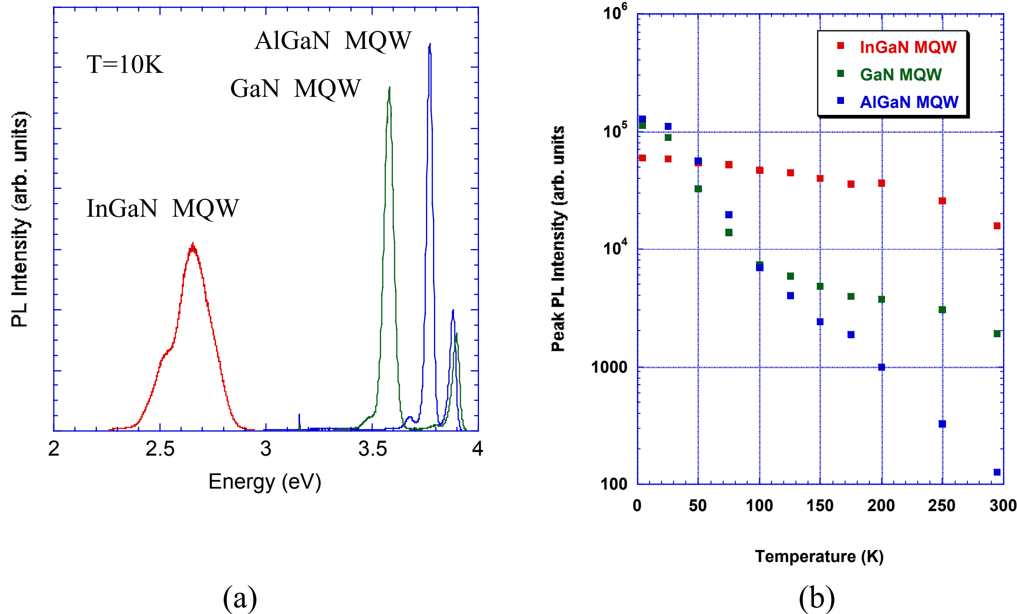

(a) (b)

Figure 23. (a) T=10K PL of InGaN, GaN and AlGaN MQWs and (b) Temperature … dependence of peak PL intensity for InGaN, GaN and AlGaN MQWs.

As a final experiment, we performed temperature dependent PL studies of InGaN MQW structures where the In composition was kept to a low value (~ 4%) to enable room temperature emission at 380 nm in the UV. These structures are similar to the MQW region of the LED heterostructures described in section 2. The particular structures grown for PL studies consisted of 10 periods of 47 Å thick InGaN (x=0.04) QWs with AlInGaN barriers. A drop of 4.8X in the integrated PL intensity from 10-300K is seen, which is comparable to that seen in the blue-emitting InGaN MQW structure described in Figure 23.

In summary, the spectroscopic studies that we have performed on InGaN bulk films and InGaN, GaN and AlGaN MQWs have shown that samples with In-containing QWs can have significantly higher optical efficiency than samples with no In in the active region. This result might suggest that GaN/AlGaN MQWs may not be intrinsically capable of performing to the level of InGaN near UV and visible MQWs. To improve the performance of GaN/AlGaN MQWs, a further measure of growing the structures on epitaxially laterally overgrown GaN to significantly reduce dislocation densities may serve to largely improve the non-radiative recombination problem. Indeed, studies by Mukai et. al. have shown that GaN/AlGaN DH LEDs had up to 2X increased output powers when this technique was employed [81].

(This page intentionally left blank.)

Design and Performance of Nitride-based UV LEDs

Internal Absorption Effects for Shorter Wavelength (λ < 370 nm) UV LEDs

In consideration of the challenges in obtaining high efficiency UV LEDs, one must also seriously consider the detrimental role played by internal absorption for UV LEDs with $\lambda < 370$ nm. At the heart of this problem is the fact that most nitride-based LEDs rely on 3-4 μm thick thick n-GaN buffer layers and ~0.1 μm thick p-GaN capping layers for good current spreading and low contact resistance. While these GaN layers are rather transparent for blue LEDs operating at 450 nm, they become strongly absorptive as the QW emission wavelength reaches 370 nm and shorter wavelengths. This effect has been described by both Mayer et. al. [82] and Mukai et al. [83]as a significant contribution to the sudden loss of optical efficiency for $\lambda < 370$ nm.

We have most clearly seen this effect in the electroluminescence (EL) spectra of AlGaN MQW LEDs operating at 340 nm. These LEDs have similar AlGaN MQW active regions to those described in section 3.1. In Figure 24, we show the EL spectrum at various injection currents. As seen at the highest current injection level, a clear delineation of the GaN absorption edge can be seen at approximately 365 nm. Fabry-Perot (F-P) oscillations exist in the spectrum for wavelengths below this absorption edge, signifying the transparency of the sample at those wavelengths. In contrast, the 340 nm peak from the AlGaN QWs is significantly reduced in intensity compared to what one would expect from the tail emission and shows no F-P oscillations. Thus, it is clear that if one needs high efficiency at these shorter wavelengths, a more transparent buffer layer, such as one consisting of higher bandgap AlGaN or AlInGaN must be employed. Progress in AlGaN buffer layers has been reported by Takeuchi et. al. [84], who have demonstrated growth of a high performance blue laser structure on an $Al_{0.06}Ga_{0.94}N$ buffer layer.

AlGaN Cladding Designs: Critical thickness Limitations and Carrier Leakage

Another challenge in the growth and design of nitride-based UV LEDs is the fact that one needs increasingly higher bandgap materials for the barrier and cladding layers. These high bandgap layers are needed to ensure sufficient carrier confinement in the quantum wells, as well as to reduce carrier (especially electron) leakage out of the active region. At present, $Al_xGa_{1-x}N$ alloys with x=0.10-0.20 are most commonly used as cladding layers in InGaN and GaN LEDs. Since AlGaN is tensile strained when grown pseudomorphically on GaN buffer layers, there is a critical thickness before dislocations and/or cracking sets in. This requirement puts a strong limitation on the thickness and composition that one may use to reduce electron leakage in the LEDs. In general, these thickness limitations are much more critical for laser diodes than for LEDs, since one needs a much thicker cladding layer to provide optical confinement. Nevertheless it is important to recognize that even for UV LEDs, one must make a compromise between the cladding composition and thickness and the optimal confinement. As will be discussed in section 5, this problem can be eliminated if one could grow high bandgap AlInGaN alloys lattice matched to GaN for cladding layers or grown structures on AlGaN buffer layers. In

this section, however, we will focus on the issues of critical thickness and carrier leakage of UV LEDs with AlGaN claddings.

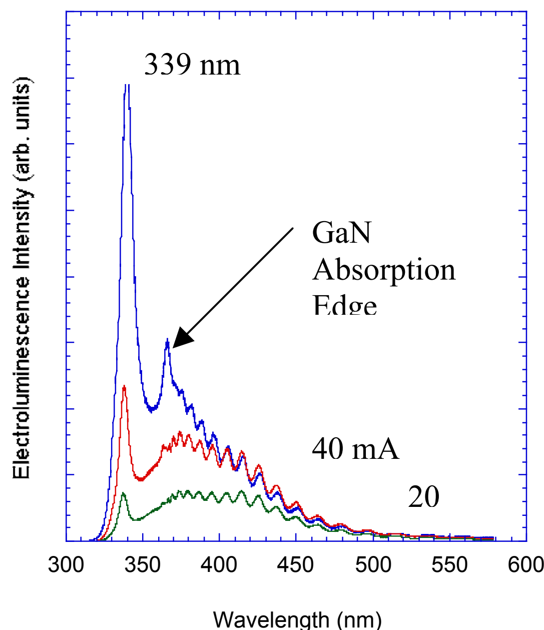

Figure 24. EL spectra for AlGaN MQW LED at various injection currents

The critical thickness of AlGaN/GaN heteostructures has been studied by Hearne, et. al. [85] through in-situ stress measurements during MOVPE growth. These stress measurements were performed using a multi-beam optical stress sensor (MOSS) which directly measures wafer curvature [86]; the wafer curvature is directly proportional to the product of the film stress and the film thickness. Using the Griffith equation described in reference 18 one can derive an approximate critical thickness of 700 Å for $Al_{0.3}Ga_{0.7}N$ epilayers on GaN , 0.15 µm for $Al_{0.2}Ga_{0.8}N$ epilayers on GaN and 0.6 µm for $Al_{0.1}Ga_{0.9}N$ epilayers on GaN. The effects of exceeding the critical thickness can be clearly seen in Figure 25, where we show a top-view photograph of a 100 µm diameter mesa-etched GaN MQW LED with $Al_{0.2}Ga_{0.8}N$ barrier and cladding layers. The total thickness of the AlGaN layers exceeds 0.2 µm. The cracking networks are especially visible in the etch-exposed n-GaN layer, where preferential etching in the cracks has made them more pronounced. I-V characterization of such LED structures yielded extremely poor reverse leakage characteristics, as shown for a number of cracked devices in Figure 25b.

Given these limitations in Al composition and thickness, it is useful to evaluate the expected carrier leakage from GaN MQW structures with various composition AlGaN claddings. We have modeled the carrier leakage in a GaN/AlGaN single QW structure grown along the c-axis of the hexagonal wurtzite crystal structure. This particular structure assumes the AlGaN layers are relaxed and that the GaN QW is compressively strained. Such a structure is relevant for UV LED structures grown on transparent AlGaN buffer layers. The basic approach is detailed in reference [87]. It involves calculating the

bandstructure and carrier distribution in both the confined QW states and the unconfined barrier states as a function of injected carrier density. Piezo-electric and spontaneous polarization effects [88] are included in the calculation. Carrier leakage is determined by assuming that the unconfined states of the QW structure, which contribute to current leakage via carrier recombination, drift or diffusion, may be populated through thermalization with the population in the bound QW states. We determine the carrier leakage by the ratio of the unconfined carrier density to the confined carrier density. A schematic of the GaN SQW heterostructure and the processes described by the model are shown schematically in Figure 26. We use a 6 x 6 Luttinger-Kohn Hamiltonian and the envelope approximation [889] to compute the hole energy dispersions and the optical dipole matrix elements. Input parameters to the calculation are the bulk wurtzite materials parameters [90] for the binary alloys. A conduction band offset of 0.67 is assumed.

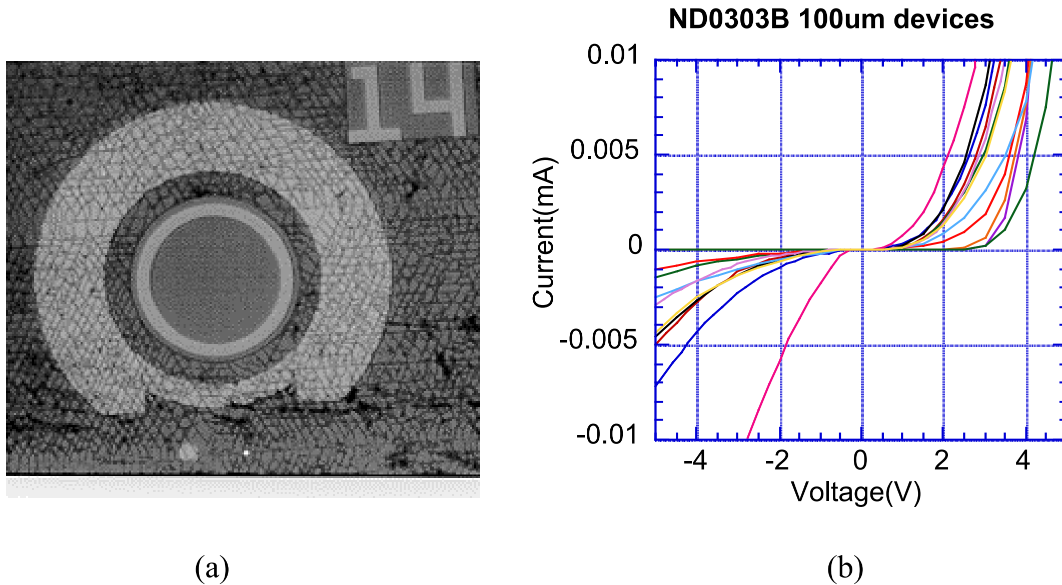

(a) (b)

Figure 25. (a) Top view photograph of a GaN /AlGaN MQW barrier and (b) I-V …. characteristics for several cracked GaN LED with > 0.2 μm total thickness of $Al_{0.2}Ga_{0.8}N$/AlGaN MQW LEDs.

We first explore the carrier leakage using a relatively low bandgap $Al_{0.1}Ga_{0.9}N$ barrier and plot the electron and hole densities in unconfined states versus total carrier population. In Figure 27 we show the results of our calculations for a 2 nm and a 4 nm thick GaN QW. The calculations assume T=300K.

For both the 2 nm QW and the 4 nm QW, we see that the unconfined carrier populations are relatively insensitive to the total carrier density until one reaches total densities of approximately $1x10^{12}$ cm^{-2}. This density is higher than that typically used for LED operation, and thus the carrier leakage should be relatively insensitive to injected

current for LED operation at modest injection levels. For UV laser diodes, however, where one would expect the threshold carrier densities to be as high as 1×10^{13} cm^{-2}, our calculations predict a significant loss of 20-35% of the carriers due to leakage. For the narrower 2 nm QW in the low injection regime (< 1×10^{12} cm^{-2}), our analysis shows that hole leakage is dominant and can represent a carrier loss of up to 20%. In contrast, electron leakage dominates for the wider 4 nm well and is reduced to ~6% at these injection levels. The dominance of hole leakage for the 2 nm well can be explained by the fact that the valence band offset is significantly smaller than the conduction band offset ($\Delta Ec=0.67Eg$ is assumed) and the confined quantum well states are relatively close to the unconfined levels in this narrow well. In the thicker 4 nm well, the confined states have lower energy relative to the unconfined states and can provide sufficient confinement for the holes. In this case, the lighter electrons experience more leakage. Although the 4 nm well is clearly superior in terms of reduced leakage, it is important to note that piezoelectric effects, which would significantly reduce electron-hole overlap, are more severe for the thicker wells.

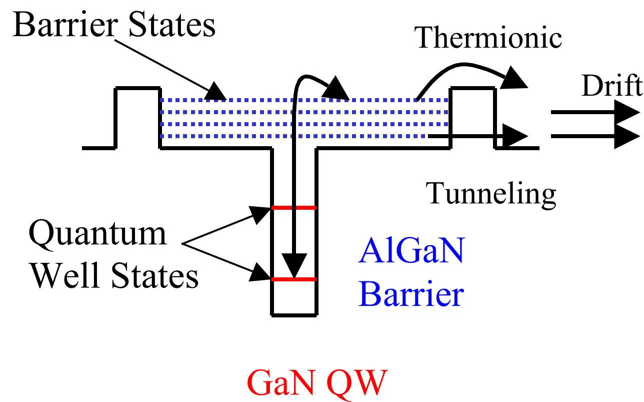

Figure 26. Schematic of the GaN SQW heterostructure and states involved in the carrier leakage model.

We further explore the importance of higher Al composition claddings by calculating the carrier leakage for 2 nm GaN QWs with $Al_{0.1}Ga_{0.9}N$ barriers and $Al_{0.2}Ga_{0.8}N$ barriers. In Figure 28, we assume an injected carrier density of 1×10^{11} cm^{-2} and plot the unconfined carrier density as a function of LED temperature. From this calculation, we see that the benefit of the higher bandgap $Al_{0.2}Ga_{0.8}N$ barrier is quite significant, showing only a 0.5% electron leakage at 300K. The stronger confinement of this structure leads to electron leakage being dominant, as for the thicker QW case in Figure 27b. The electron and hole leakage levels increase strongly with temperature, resulting in up to 2.7% electron leakage at 100ºC above room temperature.

We have shown that carrier leakage can significantly reduce the efficiency of GaN/AlGaN MQW LEDs. A barrier Al composition of x=0.2 is sufficient to reduce carrier leakage to < 1% of the total carrier population for 2 nm thick GaN QWs at 300K. In-situ stress measurements suggest that up to 0.15 μm of $Al_{0.2}Ga_{0.8}N$ barrier and cladding

layers can be employed before large scale cracking sets in. For shorter wavelength UV LEDs (< 350 nm), such as those employing AlGaN QWs, issues of carrier confinement and critical thickness are more critical.

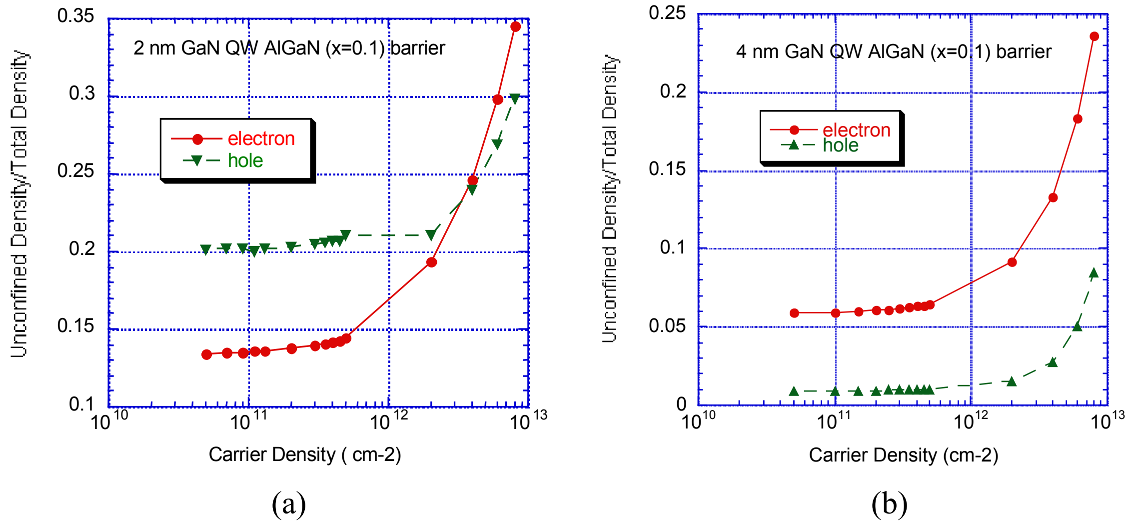

(a) (b)

Figure 27. Electron (solid curve) and hole (dashed curve) densities in unconfined states versus total (confined and unconfined) carrier population at T=300K for (a) 2 nm GaN QW/$Al_{0.1}Ga_{0.9}N$ barrier structure and (b) 4 nm GaN QW/$Al_{0.1}Ga_{0.9}N$ barrier structure.

(a) (b)

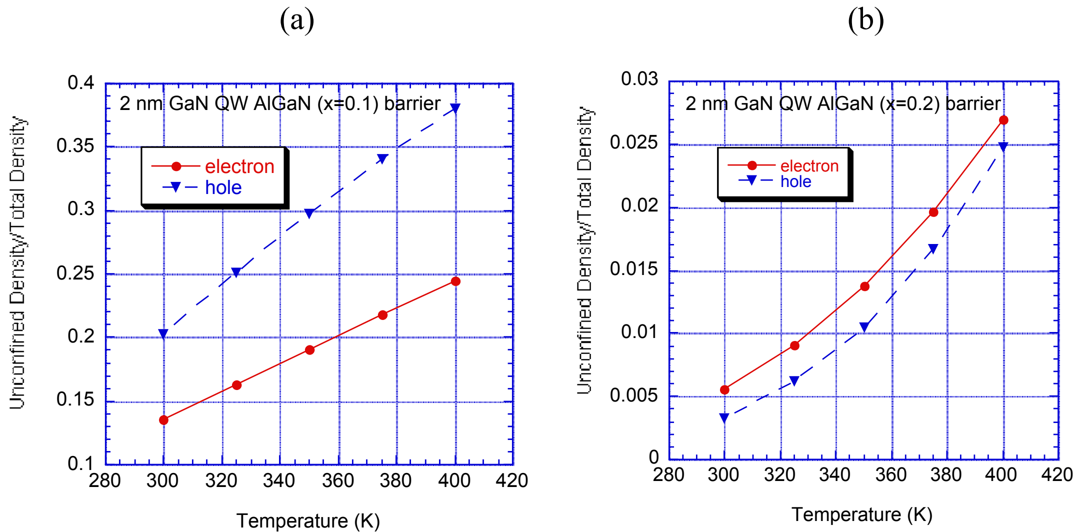

Figure 28. Electron (solid curve) and hole (dashed curve) densities in unconfined ….. states versus total (confined and unconfined) carrier population as a function of temperature for (a) 2 nm GaN QW/A $l_{0.1}Ga_{0.9}N$ barrier structure and (b) 2 nm GaN QW/$Al_{0.2}Ga_{0.8}N$ barrier structure. A total carrier concentration of $1x10^{11}$ cm^{-2} was assumed.

Performance of GaN/AlGaN MQW LEDs for λ < 360 nm

We have fabricated GaN/AlGaN MQW LEDs using the heterostructure design shown described in section 2. 100 μm-250 μm mesas were defined by inductively coupled

plasma (ICP) etching. Ti/Al/Ti/Au was used as the n-contact, and Ni/Au oxidized to form semi-transparent NiO [91] was used as the p-contact. Initial structures had a relatively narrow 30 Å QW, and electroluminescence peaked at 354 nm [72], as shown in Figure 29a. Th L-I-V data shown in Figure 29b was taken with a calibrated Si detector in close proximity to the sample, and demonstrates 13 μW of output power at a current of 20 mA (~ 180 A/cm^2 for these devices), and a turn-on voltage of approximately 4V. This performance results in an external quantum efficiency of below 0.1%, which is largely due to the internal absorption effects. The EL FWHM of 5.8 nm is significantly narrower than that reported for InGaN blue and green LEDs; a feature which is often desirable for spectroscopic applications.

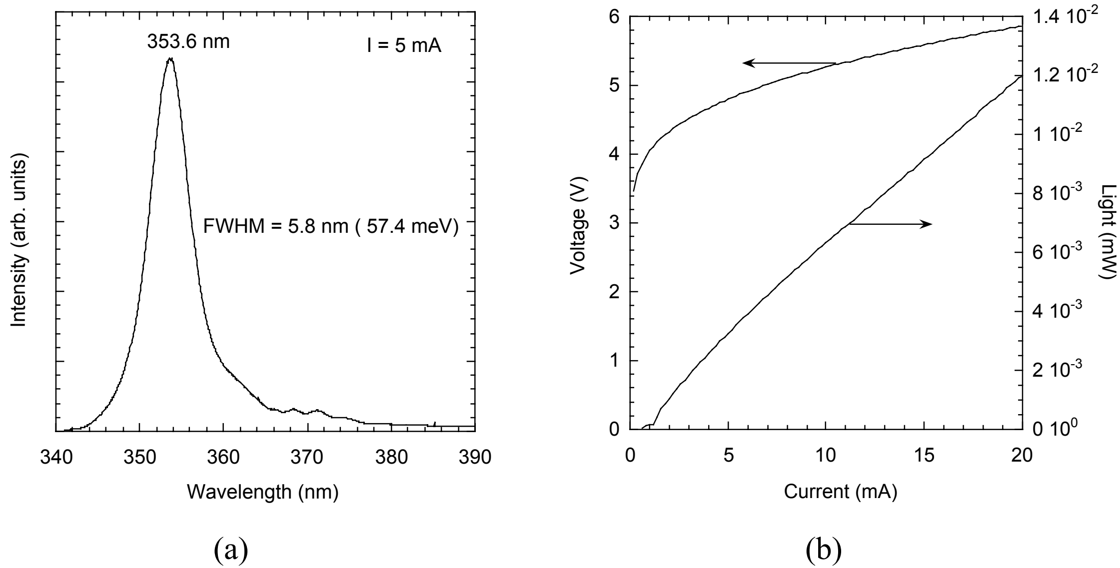

Figure 29. (a) Electroluminescence spectrum of 30 Å GaN/AlGaN MQW LED at 5 ... mA. (b) Light output-current-voltage characteristic for this 120 μm diameter mesa-etched device.

We have further optimized the growth of the GaN QW regions as well as explored QW structures emitting at slightly longer wavelengths where the internal absorption effects would be reduced. In Figure 30, we show the performance of a GaN/AlGaN MQW LED with emission at 357.5 nm. From the EL spectrum, and one can see that the tail of the spectrum is enhanced due to the strongly reduced absorption of the GaN buffer layer at those wavelengths. The L-I data shown in Figure 30b was taken from LEDs bonded to TO-headers (no encapsulation or lens), and using an integrating sphere coupled to a calibrated Si detector. These LEDs showed > 100 μW output at currents up to 50 mA (~ 100 A/cm^2 for these larger devices). While these powers are at least an order of magnitude less than that measured from commercially available blue and green LEDs, such powers are already sufficient for a number of fluorescence-based sensing applications.

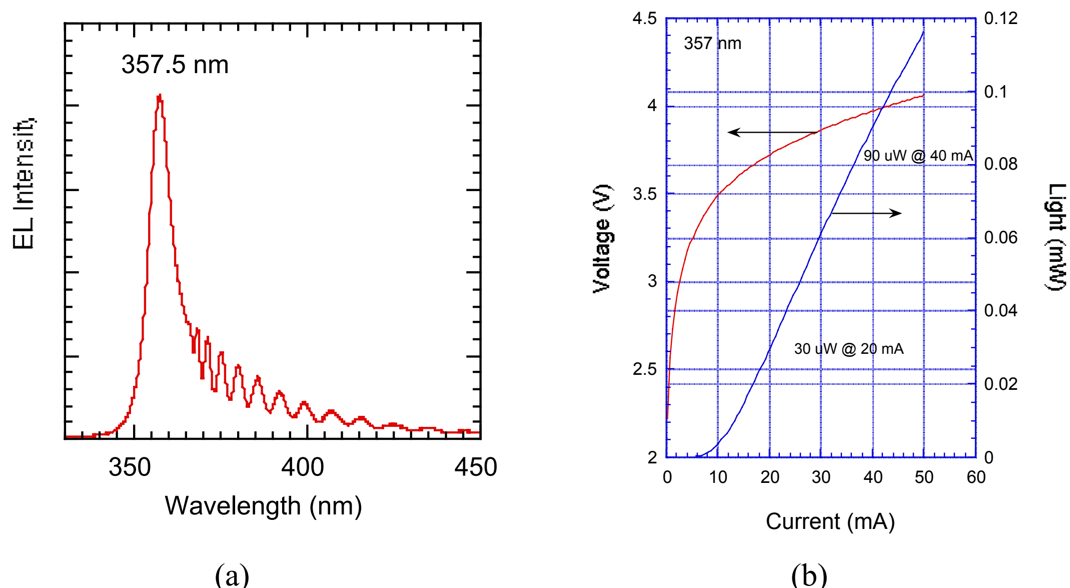

Figure 30. (a) Electroluminescence spectrum of a GaN/AlGaN MQW LED at 20 mA. (b) Light output-current-voltage data for this device.

Performance of InGaN/AlInGaN LEDs for 370 nm < λ < 390 nm

We have further explored UV LEDs employing AlInGaN quaternary alloys in the active region. These materials offer a great deal of flexibility in that they can be lattice matched to GaN and AlGaN buffer layers and thus critical thickness and cracking issues may be eliminated. Despite the obvious benefits of these quaternary alloys, the materials growth is quite challenging due partly to very dissimilar optimal temperatures for Al and In incorporation. As a result, very few reports have been made on the growth and optical properties of these materials [92]. The buffer and cladding layer designs are similar to GaN/AlGaN MQW structures, but active region consists of 47 Å thick $In_xGa_{1-x}N$ quantum wells with x=0.04 and 48 Å thick $Al_yIn_xGa_{1-x-y}N$ barriers with x=0.04 and y=0.14. This quaternary alloy composition has been found to have a room temperature PL peak at ~357 nm. As described in section 3.1, we have found that active regions consisting of this quantum well structure have very good optical efficiency.

In Figure 31, we show the electroluminescence spectrum and L-I-V data for a InGaN/AlInGaN MQW LED. The EL spectrum, taken at 20 mA, shows a peak at approximately 386 nm and a FWHM of 10 nm (84 meV). The Fabry-Perot oscillations seen throughout the spectrum indicate that these longer wavelengths experience relatively little absorption from the GaN layers in the structure. The L-I-V data, taken on devices bonded to a TO-header and using an integrating sphere and calibrated Si detector, show 0.5 mW at 50 mA (~100 A/cm^2) and greater than 1 mW powers at current levels of 100 mA (~ 200 A/cm^2). The peak external quantum efficiency of these devices is approximately 0.3%. Work is in progress to optimize growth and design of these structures to achieve higher operating efficiencies.

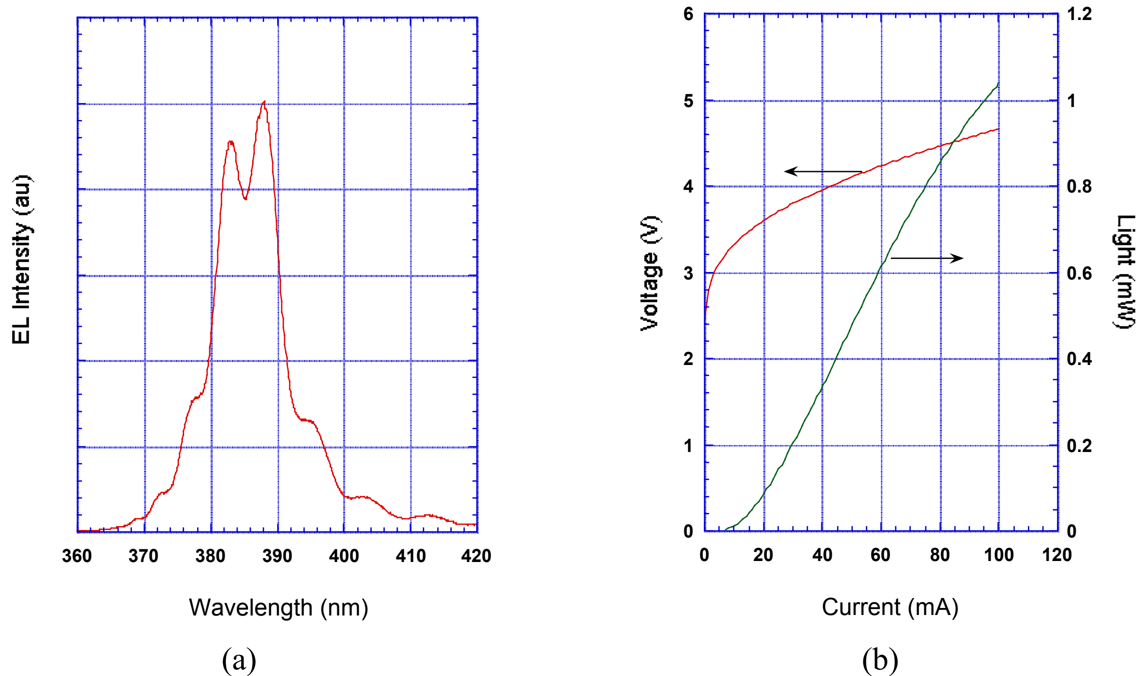

Figure 31.

We have studied a number of critical issues that must be addressed to achieve high efficiency UV LEDs. The issue of optical efficiency of UV active regions was explored through photoluminescence studies of InGaN. GaN and AlGaN bulk epilayers and MQW structures. Our results suggest that improved optical efficiency is achieved for active regions including In-containing alloys. Through a carrier leakage model that determined the percentage of carriers in unconfined states of a GaN SQW structure, we determined that $Al_{0.2}Ga_{0.8}N$ claddings provide relatively good carrier confinement for 2 nm GaN QW structures. We presented performance data for GaN/AlGaN MQW LEDs with emission in the 354-358 nm region. Output powers > 100 µW have been achieved, which is sufficient for a number of fluorescence-based sensing applications. A new InGaN/AlInGaN MQW UV LED was described which demonstrated > 1 mW output powers at an emission wavelength of 386 nm. Further optimization of this structure may provide a high efficiency near-UV source suitable for phosphor excitation and white light generation.

AlGaN/GaN HEMTs

Solid-state electronics have continually gained ground against vacuum tubes since they were first introduced almost 50 years ago due to their well known advantages in size, cost, and reliability. Vacuum devices such as traveling wave tubes (TWT) are still used in some niche applications such as high frequency power amplifiers at X-band and above, since solid-state devices such as GaAs and InP electronics do not match their power output. At these higher frequencies, power combining for solid-state devices becomes difficult at powers much above a few watts due to phase matching issues. In addition, thermal issues are difficult to deal with as the device blocks are moved closer together. Nevertheless, there remains great interest in higher power solid-state electronics in order to enhance performance and miniaturize radars and communications systems.

GaN electronics offer the potential for much higher power levels than conventional semiconductors due to a combination of better thermal properties, higher charge densities in the AlGaN/GaN quantum-well, and higher breakdown fields. A number of groups have been able to demonstrate GaN HEMT power levels in excess of 5W/mm [93-95], which can help alleviate the power combining issues. Another advantage of using GaN-based electronics is that its device impedance matching solutions become easier and more compact when the device is operated at higher drain voltages. Because of their order of magnitude higher breakdown field, GaN devices can be operated at drain voltages approximately 5x higher than GaAs at a comparable gate-drain spacing without incurring a degradation of microwave performance. The high quantum-well charge densities of AlGaN/GaN greatly exceed those for GaAs or InP-based quantum-wells because of piezoelectrically induced charge [96].

In spite of laboratory power output levels approaching 10x better than GaAs, GaN HEMTs are still limited by several important shortcomings. Lack of a lattice-matched substrate has resulted in growth of material with high defect density of $> 10^8$ cm^{-2}. For reasons that are not well understood, these defects or other types of traps are thought to lead to current collapse and related effects where microwave current levels are significantly lower than DC levels and are thought to lead to poor linearity, efficiency, gain compression, and perhaps impact reliability as well. Power-added efficiency is a critical issue for GaN HEMTs because of the need for greater heat dissipation for less efficient devices. TWTs are approximately 40% efficient at X-band. GaN devices that are less efficient may not result in any significant size reductions at the system level due to the difficulty of providing extra cooling capacity in a compact form. Conversely, TWTs are a mature technology and any improvements in GaN HEMT efficiency above 40% will lead to greater system size reduction from less cooling needs. For these reasons, many groups continue to engage in GaN HEMT research and development and to search for fundamental understandings of material-HEMT interactions.

GaN HEMT structures were grown by metalorganic chemical vapor deposition (MOCVD) on sapphire. In spite of sapphire's poor thermal properties compared to SiC, much GaN HEMT research will continue with sapphire substrates due to the high cost, limited wafer diameter, and variability of semi-insulating SiC. The HEMT structure consisted of the following layers: a 20 nm AlGaN nucleation layer, a 1.0 μm thick GaN buffer, a 3 nm undoped AlGaN layer with 20% Al, a 20 nm AlGaN layer doped with Si to $1.0x10^{18}$ cm^{-3}, and an undoped 20 nm thick AlGaN layer. Hall measurements indicated a sheet charge of $1.9x10^{13}$ cm^{-2} and a mobility of 1040 cm^2/Vs. The HEMTs were fabricated with a three step process consisting of mesa isolation with a Cl-based ICP (inductively coupled plasma) etch followed with a Ti/Al/Pt/Au (25/100/45/150 nm) ohmic contact alloyed at 850ºC for 30 s, and a Ni/Au mushroom gate defined by electron beam lithography. Gate lengths of 0.1, 0.25, and 0.5 μm were printed on each wafer. The source-drain spacing was 3.5 μm. All testing was done on-wafer without any cooling.

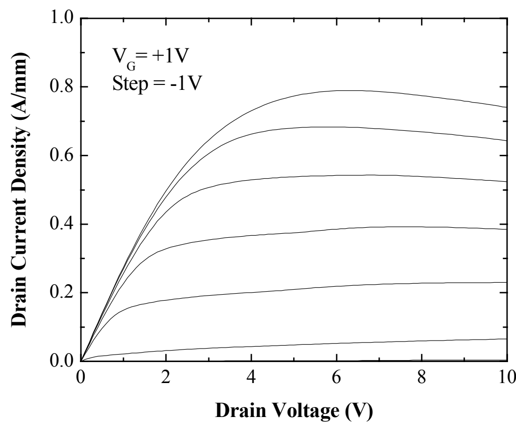

Figure 32. Drain I-V characteristics for a $0.25x150$ μm^2 GaN HEMT.

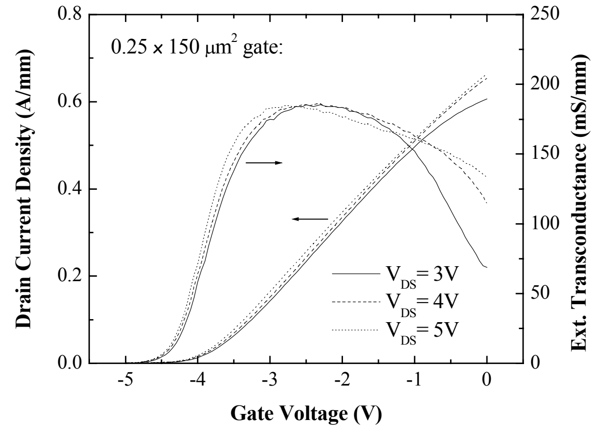

Figure 33. Drain I-V and g_m for a $0.25x150$ μm^2 GaN HEMT.

The DC current-voltage curves for a $0.25x150$ μm^2 HEMT are plotted in Figure 32 for a gate bias of 1.0 V stepping in –1 V increments until the device pinches off. The threshold voltage is approximately –4.2 V. A maximum current level of 0.8 A/mm was achieved for a 1 V gate bias. For drain bias less than 10 V, no current collapse effects are noted in the DC data. Slight self-heating effects are noted from the negative differential resistance as seen in Figure 32. The effect becomes more pronounced at drain biases between 10 and 20 V. Current-voltage plots as a function of gate bias for three drain biases are shown in Figure 33. A maximum transconductance (g_m) of 187 mS/mm was measured. Transconductance plots for 0.1, 0.25, and 0.5 μm gate lengths are shown in Figure 34. The HEMT with a 0.1 μm gate length showed the best g_m of 207 mS/mm, although it also exhibits more short channel effects than longer gate length HEMTs. The 0.25 and 0.5 μm gate length devices show a broad and nearly flat g_m profile, which

should provide a larger gate voltage swing and thereby improve the dynamic range for power and linearity.

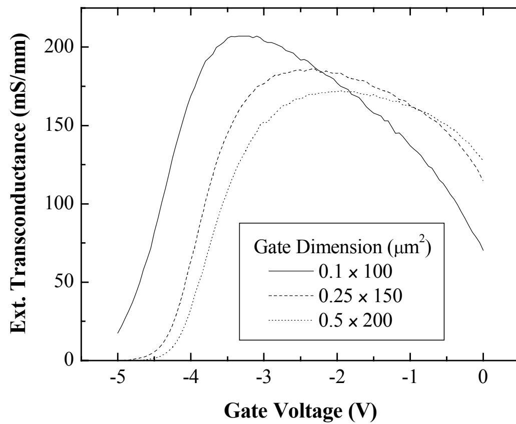

Figure 34. Transconductance plots for 0.1, 0.25, and 0.5 μm gate length GaN HEMTs.

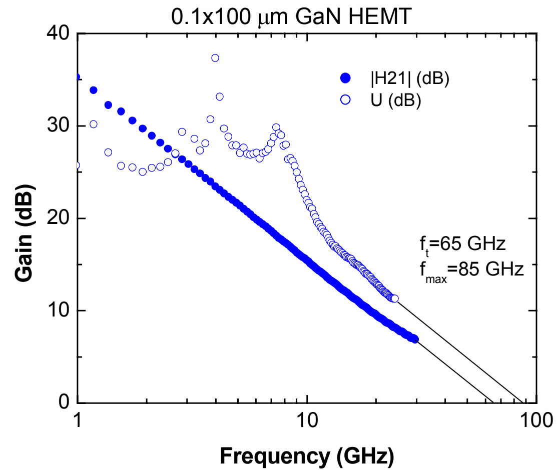

Figure 35. Measured cutoff frequency and maximum frequency of oscillation for 0.1x100 μm^2 GaN HEMTs.

The small signal s-parameters were measured with a 8510 network analyzer. From this data the short circuit current gain (h_{21}) and the Mason's unilateral gain (U) are plotted in Figure 35 for a 0.1x100 μm GaN HEMT biased at V_{DS}=4V and I_{DS}=200mA/mm. These are conditions that do not cause significant heating as seen in Figure 32. The data was extrapolated using a 20 db/decade rolloff, from which a cutoff frequency (f_t) of 65 GHz a maximum frequency of oscillation (f_{max}) of 85 GHz were extracted, both of which are extrinsic values uncorrected for pad parasitics. F_t and f_{max} are plotted as a function of gate length in Figure 36. The f_t – gate length product ranged from 7-10 GHz-μm. This value is at the low end of reported values, probably due to the relatively large source-drain spacing used in this work.

Microwave power measurements were made on-wafer at 3 GHz without cooling using an ATN load pull system for a 0.25 x 150 μm^2 device. This device was chosen instead of the 0.1 μm HEMT due to the flatter g_m profile and reduced short channel effects. Although the breakdown voltage was higher than 40 V, the poor thermal properties of sapphire limited the bias conditions to V_{DS}=14 V and I_{DS}=385 mA/mm. The output power, gain, and efficiency are plotted in Figure 37. The linear gain was 20 dB. At the 3 dB compression point, an output power of 26.2 dbm (413 mW) was achieved, yielding an output power density of 2.75 W/mm and a power-added efficiency of 56% with 17 dB gain. Device performance degraded with higher drain bias. At 10 GHz, the device was biased at V_{DS}=18 V and I_{DS}=345 mA/mm and the output power was measured at 23.96 dBm (248mW). The power density at the3 db gain compression point was 1.66 W/mm with 27% power-added efficiency and 10 dB gain.

These unpassivated GaN HEMT results are competitive with other small periphery HEMTs fabricated on uncooled sapphire substrates. The ohmic contact resistance of 0.3 Ω-mm is among the lowest achieved in HEMTs of any Al composition. For example, Binari et al. [97] achieved a higher CW output of 3.3 W/mm with the same gate width (150 μm) at 3.8 GHz for a passivated HEMT with lower power-added efficiency (45%) and gain (10 dB). SiN passivation has been shown to increase the breakdown voltage and increase the output power level of GaN HEMTs [98] and will be incorporated into our devices in the near future.

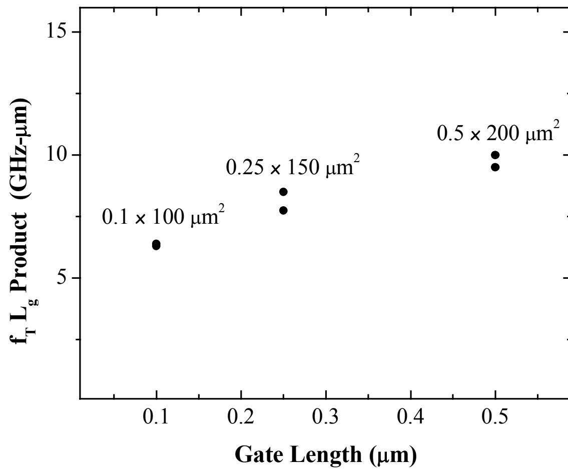

Figure 36. Gate length-ft product for various GaN HEMTs.

SG:SEL:NS:1;R:1;IC:S#:6;
LG:SEL:NS:1;R:1;OC:S#:99755;
Power Out vs Power In

Frequency (f0): 3 GHz
Vg -1.000 V
Vd 14.001 V
Bias #: 1

Source State: 1 # 6
Source Gamma: .76 14.5
Load State: 1 # 99755
Load Gamma: .57 -5.7

Pout @ 1 dB: 22.524
Gain @ 1 dB: 19.16
Eff @ 1 dB: 20.562
Pout @ 3 dB: 26.155
Gain @ 3 dB: 17.17
Eff @ 3 dB: 56.24

Power Out
Efficiency
Gain

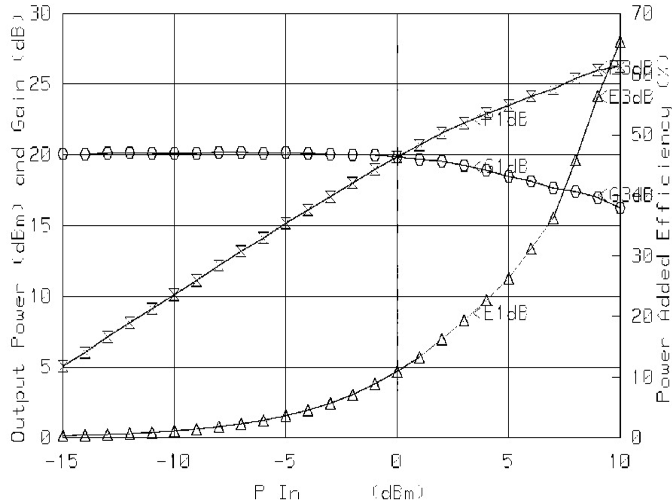

Figure 37. Microwave power performance of a 0.25x150 μm^2 GaN HEMT at 3 GHz.

A thermal simulation for a similar geometry and thermal load allows us to estimate the channel temperature range of 300-350ºC under high current stress [99]. Such a high temperature will limit the transport properties which will saturate power output and reduce gain and efficiency. Although these devices are thermally limited, power output results still provide a useful metric because increased efficiency is a

fundamental goal of this type of work and device designs that lead to better efficiency will readily lead to higher output power before the thermal limit is reached.

In conclusion, GaN HEMT structures were grown and fabricated on sapphire substrates by MOCVD. DC and rf results are comparable to other reported GaN HEMTs on uncooled sapphire substrates with current density in excess of 0.8 A/mm, f_t of 65 GHz, f_{max} of 85 GHz, and power density of 1.66 W/mm at 10 GHz. This device technology is now ready to be used with cantilever epitaxy material for high performance HEMTs on reduced defect density substrates.

(This page intentionally left blank.)

References

[1] C.I.H. Ashby, C.C. Willan, Jung Han, N.A. Missert, P.P. Provencio, D.M. Follstaedt, G.M. Peake, and L.Griego, Appl. Phys. Lett. 77, 3233 (2000).

[2] M.E. Coltrin, C.C. Willan, M.E. Bartram, J. Han, N. Missert, M.H. Crawford, A.G. Baca, MRS Internet J. Nitride Semicond. Res. 4S1, G6.9 (1999).

[3] K. Hiramatsu, T. Detchprohm, and I. Akasaki, Jpn. J. Appl. Phys., **32**, 1528 (1993).

[4] T. Detchprohm, K. Hiramatsu, K. Itoh, and I. Akasaki, Jpn. J. Appl. Phys., **31**, 1454 (1992).

[5] W. G. Perry, M. B. Bremser, T. Zheleva, K. J. Lithicum, and R. F. Davis, Thin Solid Films, **324**, 107 (1997).

[6] J. Qu, J. Li, and G. Zhang, Solid State Communications, **107**, 467 (1998).

[7] I. Akasaki, and H. Amano, Jpn. J. Appl. Phys., **36**, 5393 (1997).

[8] S. Hearne, E. Chason, J. Han, J. A. Floro, J. Figiel, J. Hunter, H. Amano, and I. S. T. Tsong, Appl. Phy. Lett., **74**, 356 (1999).

[9] J. A. Floro, E. Chason , and S. R. Lee Mater. Res. Soc. Symp. Proc. **406**, 491 (1996).

[10] Cracks were occasionally observed to lie on inclined planes when viewed in cross-section.

[11] K. Ito, K. Hiramatsu, H. Amano, and I. Akasaki, J. Cryst. Growth, **104**, 533 (1990).

[12] K. Wang, and R. Reeber, Mat. Res. Soc. Symp. Proc., **482** (1997).

[13] J. H. Selverian, and D. O'Neal, Thin Solid Films **235**, 120 (1993).

[14] For hexagonal symmetry: $\nu = [C_{13}/(C_{11}-C_{12})]$; $M_{(0001)} = C_{13}+C_{12}-2[C_{11}^2/C_{33}]$; $G_f = C_{66}$ where C_{ij} are elements of the stiffness matrix.

[15] A. Polian, M. Grimsditch, and I. Grzegory, J. Appl. Phys., Part 1 **27**, L1384 (1988).

[16] *Landolt-Börnstein Numerical Data and Functional Relationships in Science and Technology*, edited by K. H. Hellwege, A. M. Hellwege, and D. F. Nelson (Springer Berlin, 1979,1992), Vols. III: 11, III: 29.

[17] J. W. Matthews, and A. E. Blakeslee, J. Cryst. Growth **27**, 118 (1974).

[18] B. Jahnen, M. Albrecht, W. Dorsch, S. Christiansen, H. P. Stunk, D. Hanser, and R. F. Davis, MRS Internet J. Nitride Semiconductor Research **3**, 39 (1998).

[19] J. W. Hutchinson, and Z. Sou, Advances in Applied Mechanics, **29**, 63-191, Academic Press, San Diego (1992).

[20] C. Wetzel, T. Takeuchi, S. Yamaguchi, H. Katoh, H. Amano, and I. Akasaki, Appl. Phys. Lett. **73,** 1994 (1998).

[21] M. D. McCluskey, C. G. Van de Walle, C. P. Master, L. T. Romano, and N. M. Johnson, Appl. Phys. Lett. **72,** 2725 (1998).

[22] J. Wagner, A. Ramakrishnan, D. Behr, M. Maier, N. Herres, M. Kunzer, H. Obloh, and K.-H. Bachem, MRS Internet J. of Nitride Semicond. Res. **4S1,** G2.8 (1999).

[23] R. Goldhahn, J. Scheiner, S. Shokhovets, T. Frey, U. Köhler, D. J. As, and K. Lischka, Appl. Phys. Lett. **76,** 291 (2000).

[24] O. Brandt, J. R. Müllhäuser, B. Yang, H. Yang, and K. H. Ploog, Physica E **2,** 532 (1998).

[25] S. Chichibu, T. Azuhata, T. Sota, and S. Nakamura, Appl. Phys. Lett. **70,** 2822 (1997).

[26] K. P. O'Donnell, R. W. Martin, and P. G. Middleton, Physical Review Letters **82,** 237-240 (2000).

[27] I. Ho and G. B. Stringfellow, Appl. Phys. Lett. **69,** 2701 (1996).

[28] C. Wetzel, T. Takeuchi, H. Amano, and I. Akasaki, J. Appl. Phys. **85,** 3786 (1999).

[29] W. W. Chow and S. W. Koch, *Semiconductor-Laser Fundamentals: Physics of the Gain Materials* (Springer, Berlin, 1999).

[30] D. Doppalapudi, S. N. Basu, K. F. Ludwig Jr., and T. D. Moustakas, J. Appl. Phys. **84,** 1389 (1998); D. Doppalapudi, S. N. Basu, and T. D. Moustakas, J. Appl. Phys. **85**, 883 (1999); M. K. Behbehani, E. L. Piner, S. X. Liu, N. A. El-Masry, and S. M. Bedair, Appl. Phys. Lett. **75**, 2202 (1999); P. Ruterana, G. Nouet, W. Van der Scricht, I. Moerman, and L. Considine, Appl. Phys. Lett. **72**, 1742 (1998); P. Ruterana and F. Deniel, Mat. Sci. and Eng. B **59**, 186 (1999).

[31] J. E. Northrup, L. T. Romano, and J. Neugebauer, Appl. Phys. Lett. **74,** 2319 (1999).

[32] P. Hohenberg and W. Kohn, Phys. Rev. **136,** B864 (1964); W. Kohn and L. J. Sham, Phys. Rev. **140**, A1133 (1965); D. M. Ceperley and B. J. Alder, Phys. Rev. Lett. **45**, 566 (1980); J. P. Perdew and A. Zunger, Phys. Rev. B **23**, 5048 (1981).

[33] G. Kresse and J. Hafner, Phys. Rev. B **49,** 14251 (1994); G. Kresse and J. Furthmüller, Comp. Mat. Sci. **6**, 15 (1996); D. Vanderbilt, Phys. Rev. B **41**, 7892 (1990).

[34] U. Grossner, J. Furthmüller, and F. Bechstedt, Phys. Rev. B **58,** R1722 (1998).

[35] H. J. Monkhorst and J. D. Pack, Phys. Rev. B **13,** 5188 (1976).

[36] A. F. Wright and J. S. Nelson, Appl. Phys. Lett. **66,** 3051 (1995).

[37] A. F. Wright and J. S. Nelson, Appl. Phys. Lett. **66,** 3465 (1995).

[38] L. Vegard, Zeitschrift für Physik **5,** 17 (1921).

[39] A. F. Wright, J. Appl. Phys. **82,** 2833 (1997).

[40] M. S. Hybertsen and S. G. Louie, Phys. Rev. B **34,** 5390 (1986).

[41] *Optical Spectroscopy and Composition of InGaN*; *Vol. 595*, edited by K. P. O'Donnell, R. W. Martin, M. E. White, K. Jacobs, W. Van der Stricht, P. Demeester, A. Vantomme, M. F. Wu, and J. F. W. Mosselmans (Materials Research Society, Boston, MA, 1999).

[42] C. G. Van de Walle, M. D. McCluskey, C. P. Master, L. T. Romano, and N. M. Johnson, Mat. Sci. and Eng. B **59,** 274 (1999); L. Bellaiche, T. Matilla, L. -W. Wang, S. H. Wei, and A. Zunger, Appl. Phys. Lett. **74**, 1842 (1999). We note that

recent all-electron calculations [M. van Schilfgaarde, A. Sher, and A. -B. Chen, J. Crystal Growth **178**, 8 (1997)] yielded results for unstrained zinc-blende alloys in

excellent agreement with our results. [1ba] For a review, see S. Nakamura and G. Fasol, *The Blue Laser Diode*, Springer-Verlag, Berlin (1997).

[43] J. Han, M. H. Crawford, R. J. Shul, J. J. Figiel, M. Banas, L. Zhang, Y. K. Song, H. Zhou, and A. V. Nurmikko, Appl. Phys. Lett, 73, 1688 (1998)

[44] J. Han, M. H. Crawford, R. J. Shul, S. J. Hearne, E. Chason, J. J. Figiel, and M. Banas, MRS Internet J. Nitride Semicond. Res. 4S1 G7.7 (1999).

[45] J. Han, T. –B. Ng, R. M. Biefeld, M. H. Crawford, and D. M. Follstaedt: Appl. Phys. Lett. **71** (1997) 3114.

[46] W-K. Chu, J. W. Mayer, and M.-A. Nicolet: *Backscattering Spectrometry* (Academic, New York, 1978).

[47] M. Mayer: *SIMNRA User's Guide*, Technical Report IPP 9/113 (Max Planck-Institut fur Plasmaphysik, Garching, Germany, 1997).

[48] C. Taylor, D. Barlett, E. Chason, J. A. Floro, Ind. Physicist 4, 25 (1998)

[49] S. Hearne, E. Chason, J. Han, J. A. Floro, J. Hunter, J. J. Figiel: Appl. Phys. Lett. **74** (1999) 356.

[50] T. Takeuchi, H. Takeuchi, S. Sota, H. Sakai, H. Amano, and I. Akasaki: Jpn. J. Appl. Phys. **36** (1997) L177; S. Nakamura and T. Mukai: J. Vac. Sci. Tech. **A 13** (1995) 705.

[51] S. Chichibu, T. Azuhata, T. Sota, and S. Nakamura: Appl. Phys. Lett. **70** (1997) 2822; S. F. Chichibu, A. C. Abare, M. P. Mack, M. S. Minsky, T. Deguchi, D. Cohen, P. Kozodoy, S. B. Fleischer, S. Keller, J. S. Speck, J. E. Bowers, E. Hu, U. K. Mishra, L. A. Coldren, S. P. DenBaars, K. Wada, T. Sota, and S. Nakamura: Mat. Sci. Eng. **B59** (1999) 298.

[52] S. Chichibu, T. Deguchi, T. Sota, K. Wada, and S. Nakamura: Mat. Res. Soc. Symp. Proc. **482** (1998) 613.

[53] O. Ambacher, J. Phys. D: Appl. Phys. 31, 2653 (1998).

[54] C. Kisielowski, J. Kruger, S. Ruvimov, T. Suski, J. W. Ager III, E. Jones, Z. Liliental-Weber, M. Rubin, E. R. Weber, M. D. Bremser, and R. F. Davis: Phys. Rev. **B 54** (1996) 17745.

[55] S. Chichibu, A. Shikanai, T. Azuhata, T. Sota, A. Kuramata, K. Horino, and S. Nakamura, Appl. Phys. Lett. 68, 3766 (1996)

[56] S. M. Bedair, *Gallium Nitride (GaN) I*, Semiconductors and Semimetals, v50, p127 (1998), Academic Press, San Diego

[57] T. Mukai, D. Morita, and S. Nakamura, J. Cryst. Growth 189/190, 778 (1998)

[58] Y. Narukawa, S. Saijou, Y. Kawakami, S. Fujita, T. Mukai, and S. Nakamura, Appl. Phys. Lett. 74, 558 (1999)

[59] X. Shen and Y. Aoyagi, Jpn. J. Appl. Phys. 38, L14 (1999).

[60] T. Matsuoka: Appl. Phys. Lett. **71** (1997) 105.

[61] F. G. McIntosh, K. S. Boutros, J. C. Roberts, S. M. Bedair, E. L. Piner, and N. A. El-Masry: Appl. Phys. Lett. **68** (1996) 40; S. M. Bedair, F. G. McIntosh, J. C.

Roberts, E. L. Piner, K. S. boutros, N. A. El-Masry: J. Cryst. Growth **178** (1997) 32.
[62] S. Yamaguchi, M. Kariya, S. Nitta, H. Kato, T. Takeuchi, C. Wetzel, H. Amano, and I. Akasaki: J. Cryst. Growth **195** (1998) 309.
[63] T. Peng, J. Piprek, G. Qiu, J. O. Olowolafe, K. M. Unruh, C. P. Swann, and E. F. Schubert: Appl. Phys. Lett. **71** (1997) 2439
[64] S. F. Chichibu, H. Marchand, M. S. Minsky, S. Keller, P. T. Fini, J. P. Ibbetson, S. B. Fleischer, J. S. Speck, J. E. Bowers, E. Hu, U. K. Mishra, S. P. DenBaars, T. Deguchi, T. Sota, and S. Nakamura: Appl. Phys. Lett. **74** (1999) 1460.
[65] A. F. Wright and J. S. Nelson: Appl. Phys. Lett. **66** (1995) 3051; A. F. Wright and J. S. Nelson: Appl. Phys. Lett. **66** (1995) 3465.
[66] K. S. Kim, A. Saxler, P. Kung, M. Razeghi, and K. Y. Lim: Appl. Phys. Lett. **71** (1997) 800.
[67] M. Leroux, N. Grandjean, B. Beaumont, G. Nataf, F. Semon, J. Massies, and P. Gibart, J. Appl. Phys. 86, 3721 (1999).
[68] Y. Narukawa, Y. Kawakami, S. Fujita, and S. Fujita, Phys. Rev. B 55, R1938 (1997).
[69] S. F. Chichibu, private communication (1999).
[70] I. Akasaki and H. Amano, Jpn. J. Appl. Phys., **36**, 5395(1997).
[71] T. Mukai, D. Morita and S. Nakamura, J. Cryst. Growth, **189/190**, 778 (1998).
[72] J. Han, M. H. Crawford, R. J. Shul, J. J. Figiel, M. Banas, L. Zhang, Y. K. Song, H. Zhou and A. V. Nurmikko Appl. Phys. Lett., **73**, 1688 (1998).
[73] E. S. Jeon, V. Kozlov, Y.-K. Song, A. Vertikov, M. Kuball, A. V. Nurmikko, H. Liu, C. Chen, R. S. Kern, C. P. Kuo and M. G. Craford, Appl. Phys. Lett., **69**, 4194 (1996).
[74] S. Chichibu, T. Azuhata, T. Sota and S. Nakamura, Appl. Phys. Lett., **70**, 2822 (1997).
[75] T. Wang, D. Nakagawa, M. Lachab, T. Sugahara, S. Sakai, Appl. Phys. Lett., **74**, 3128 (1999) and references therein.
[76] S.F.Chichibu, A.Shikanai, T.Deguchi, A.Setoguchi, R.Nakai, H.Nakanishi, K.Wada, S.P.DenBaars, T.Sota, and S.Nakamura, Jpn. J. Appl. Phys. **39**, Part 1 (2000) (to be published)
[77] Y. Narukawa, S. Saijou, Y. Kawakami, S. Fugita, t. Mukai, S. Nakamura, Appl. Phys. Lett., **74**, 558 (1999).
[78] H. Kumano, K. Hoshi, S. Tanaka, I. Suemune, X. Q. Shen, P. Riblet, P. Ramvall and Y. Aoyagi, Appl. Phys. Lett., **75**, 2879 (1999).
[79] V. Fiorentini, F. Bernadini, Phys. Rev. B, **60**, 8849 (1999).
[80] M. Leroux, N. Grandjean, B. Beaumont, G. Nataf, F. Semond, J. Massies, P. Gibart, J. Appl. Phys., **86**, 3721 (1999).
[81] T. Mukai and S. Nakamura, Jpn. J. Appl. Phys., **38**, 5735 (1999).
[82] M. Mayer, A. Pelzmann, C. Kirchner, M. Schauler, F. Eberhard, M. Kamp, P. Unger and K. J. Ebeling, J. Cryst. Growth, **189/190**, 782 (1998).
[83] T. Mukai, M. Yamada and S. Nakamura, Jpn. J. Appl. Phys.,**37**, L1358 (1998).

[84] T. Takeuchi, T. Detchprohm, M. Iwaya, N. Hayashi, K. Isomura, K. Kimura, M. Yamaguchi, H. Amano, I. Akasaki, Yw. Keneko, R. Shioda, S. Watanabe, T. Hidaka, Y. Yamaoka, Ys. Kaneko and N. Yamada, Appl. Phys. Lett., **75**, 2960 (1999).

[85] S. J. Hearne, J. Han, S. R. Lee, J. A. Floro, D. M. Follstaedt, E. Chason and I. S. T. Tsong, Appl. Phys. Lett. (to be published)

[86] J. A. Floro, E. Chason and S. R. Lee, Mater. Res. Soc. Symp. Proc. **406**, 491 (1996).

[87] W. W. Chow, M. Hagerott Crawford, A. Girndt and S. W. Koch, IEEE J. Sel. Topics in Quant. Electron., **4**, 514 (1998).

[88] O. Ambacher, J. Smart, J. R. Shealy, N. G. Weimann, K. Chu, M. Murphy, W. J. Schaff, L. F. Eastman, R. Dimitrov, L. Wittmer, M. Stutzmann, W. Rieger and J. Hilsenbeck, J. Appl. Phys., **85**, 3222 (1999).

[89] S. L. Chuang and C. S. Chang, Phys. Rev. B, **54**, 2491 (1996).

[90] W. W. Chow and S. W. Koch, *Semiconductor-Laser Fundamentals*, Chapter 6, Springer-Verlag, Berlin, 1999.

[91] Jin-Kuo Ho; Charng-Shyang Jong; Chiu, C.C.; Chao-Nien Huang; Kwang-Kuo Shih; Li-Chien Chen; Fu-Rong Chen; Ji-Jung Kai, J. Appl. Phys., **86**, 4491 (1999).

[92] M. E. Aurner, S. F. LeBoeuf, F. G. McIntosh and S. M. Bedair, Appl. Phys. Lett., **75**, 3315 (1999).

[93] S. T. Sheppard, K. Doverspike, W.L. Pribble, S. T. Allen, J. W. Palmour, L. T. Kehias, and T. J. Jenkins, IEEE Electron Device Lett. **20**, 161 (1999).

[94] J. S. Moon, M. Micovic, P. Janke, P. Hashimoto, W.-S. Wong, R. D. Widman, L. McCray, A. Kurdoghlian, and C. Nguyen, Electron. Lett. **37**, 528 (2001).

[95] S. Keller, Y.-F. Wu, G. Parish, N. Ziang, J. J. Xu, B. P. Keller, S. P. DenBaars, and U. K. Mishra, IEEE Electron Trans. Electron. Dev. **48**, 552 (2001).

[96] M. S. Shur, R. Gaska, and A. Bykhovski, , Solid-State Electron. **41**, 1451 (1997).

[97] S. C. Binari, K. Ikossi, J. A. Roussos, W. Kruppa, D. Park, B. Dietrich, D. D. Koleske, A. E. Wickenden, and R. L. Henry, IEEE Electron Trans. Electron. Dev. **48**, 465 (2001).

[98] B. M. Green, K. K. Chu, E. M. Chumbes, J. A. Smart, J. R. Shealy, and L. F. Eastman, IEEE Electron Device Lett. **21**, 268 (2000).

[99] Y.-F.Wu, B. P. Keller, D. Kapolnek, P. Kozodoy, S. P. Denbaars, and U. K. Mishra, Solid-State Electron. **41**, 1569 (1997).

DISTRIBUTION

2	Albert G. Baca, 1742	0603
1	Ronald D. Briggs, 1742	0603
1	Randy J. Shul, 1763	0603
1	Andrew A. Allerman, 1126	0601
1	A. J. Fischer, 1123	0601
1	Christine C. Mitchell, 1126	0601
1	D. D. Koleske, 1126	0601
1	S. R. Kurtz, 1123	0601
1	A. F. Wright, 1112	1415
1	C. I. H. Ashby, 1744	1425
2	Robert M. Biefeld, 1126	0601
1	Charles A. Sullivan, 1740	0603
1	T. E. Zipperian, 1740	1077
1	D. R. Myers, 1700	1071
1	J. M. Phillips, 1100	1427
1	LDRD Office, 1030	0188
1	Central Technical Files, 8945-1	9018
2	Technical Library, 9616	0849
1	Review and Approval Desk, 9612 for DOE/OSTI	0612